First-principles materials applications and design of nonlinear optical crystals

2014 J. Phys. D: Appl. Phys. 47 253001

(http://iopscience.iop.org/0022-3727/47/25/253001)

IOP Publishing Journal of Physics D: Applied Physics

J. Phys. D: Appl. Phys. **47** (2014) 253001 (19pp) doi:10.1088/0022-3727/47/25/253001

Topical Review

First-principles materials applications and design of nonlinear optical crystals

Zheshuai Lin[1], Xingxing Jiang[1,3], Lei Kang[1,3], Pifu Gong[1,3], Siyang Luo[1] and Ming-Hsien Lee[2]

[1] Beijing Center for Crystal R&D, Key Laboratory of Functional Crystals and Laser Technology of the Chinese Academy of Sciences, Technical Institute of Physics and Chemistry, Chinese Academy of Sciences, Beijing 100190, People's Republic of China
[2] Department of Physics, Tamkang University, Tamsui, Taipei 251, Taiwan
[3] University of the Chinese Academy of Sciences, Beijing 100049, People's Republic of China

E-mail: zslin@mail.ipc.ac.cn

Received 2 March 2014, revised 9 April 2014
Accepted for publication 10 April 2014
Published 23 May 2014

Abstract

With the development of laser technology and related scientific fields, understanding of the structure–property relationships in nonlinear optical (NLO) crystals is becoming more and more important. In this article, first-principles studies based on density functional theory, and their applications to elucidate the microscopic origins of the linear and NLO properties in NLO crystals, are reviewed. The *ab initio* approaches have the ability to accurately predict the optical properties in NLO crystals, and the developed analysis tools are vital to investigating their intrinsic mechanism. This microscopic understanding has further guided molecular engineering design for NLO crystals with novel structures and properties. It is anticipated that first-principle material approaches will greatly improve the search efficiency and greatly help experiments to save resources in the exploration of new NLO crystals with good performance.

Keywords: first-principles studies, nonlinear optical crystals, structure–property relation, molecular engineering design

(Some figures may appear in colour only in the online journal)

1. Introduction

Half a century ago Franklin first observed optical second harmonic generation (SHG) signals in SiO_2 [1] almost immediately after the invention of the laser at the beginning of the 1960s. Since then materials exhibiting large nonlinear optical (NLO) responses have attracted more and more attention because of their wide applications in laser sciences and technology. Now the NLO materials have played an important role as a key device in the all-solid-state lasers used in areas such as ultrafine spectrum analysis, precise micro-manufacturing, large screen displays, remote communications, and medical diagnosis [2–8]. The search for new NLO crystals, particularly for the ultraviolet (UV) and infrared (IR) spectral regions, is very active [9–17], even though intensive efforts in this field have been in progress for more than three decades.

The performance of an SHG crystal is mainly determined by its abilities to double the frequency of a laser beam. To achieve noticeable SHG output, an NLO crystal must have a large enough birefringence Δn to achieve the phase-matching condition. Strictly speaking, the phase-matching condition requires an appropriate wavelength dispersion of refractive indexes n_x, n_y, and n_z, i.e., $n_{\max}(\lambda) - n_{\min}(\lambda/2) > 0$ [18], where $n_{\max}(n_{\min})$ is the largest (smallest) refractive index and λ is the wavelength of the fundamental wave. This means that the birefringence $\Delta n = n_{\max}(\lambda) - n_{\min}(\lambda)$ must be larger than the difference between $n_{\min}(\lambda/2)$ and $n_{\min}(\lambda)$. Usually the dispersion curves of refractive indices are steep in the UV region but flat in the IR region. Thus, typically the birefringence that satisfies the SHG phase-matching condition becomes larger and larger as the harmonic wavelength varies from IR to UV regions. In general, the birefringence should be

larger than 0.06 for a UV SHG crystal (and larger than 0.075 for deep-UV SHG), while it could be much smaller (e.g. ∼0.03) for an IR NLO crystal. A too large birefringence, however, is not desirable either, since it would cause destructive optical behaviours such as self-focus and large walk-off effect in the conversion process [19]. It should be emphasized that actually the harmonic generation can also be fulfilled by the quasi-phase-matching method [20, 21], which can significantly reduce the requirement of birefringence, but the very complicated manufacturing and operating processes in this technique heavily hinder its practical applications; the relevant NLO materials will not be considered in this review.

Under the non-depleted pump approximation, the SHG conversion efficiency η of a crystal is given by the following expression if the phase-matching condition is satisfied [22]:

$$\eta = \frac{P_2}{P_1} = \frac{2\pi^2 d_{\text{eff}}^2 L^2 P_1}{\varepsilon_0 c n_1^2 n_2 \lambda_2^2 A} \tag{1}$$

where d_{eff} is the effective SHG coefficient of the crystal in the phase-matching direction, L is the optical path in the crystal, ε_0 is the vacuum permittivity, c is the speed of light in vacuum, n_i is the refractive index of light with wavelength λ_i, A is the sectional surface area of the laser with the fundamental wave, and P_i is the corresponding power of the λ_i beams. Formula (1) shows that in order to obtain high SHG output P_2 two key factors (besides the birefringence) should be considered, as follows.

(i) High power density of input fundamental wave, P_1/A. This requires the NLO crystal to possess high laser damage threshold (LDT). It is well known that the magnitude of LDT is closely associated with the energy bandgap in a crystal (see figure 1), mainly due to the effects of two-photon absorption or multi-photon absorption. Thus, a larger energy bandgap is beneficial to the acquirement of higher LDT. Meanwhile, a larger energy bandgap can obtain a shorter SHG wavelength and hence expand the frequency conversion range in an NLO crystal.

(ii) Large ratio of d_{eff}/λ_2. This indicates that a larger effective NLO coefficient can result in higher SHG conversion efficiency. In addition, for NLO applications in different spectral regions the requirement of the magnitude of the effective SHG coefficient is different. In order to obtain the same conversion efficiency, the SHG coefficient for a crystal in the IR region ($\lambda_2 > 900$ nm) should be one or even two orders of magnitude larger than that in the deep-UV region ($\lambda_2 < 200$ nm). In general, an SHG coefficient approximately equal to that of KH_2PO_4 (KDP, $d_{36} = 0.39\,\text{pm V}^{-1}$) is enough for practical applications in UV and deep-UV regions, but the NLO effect should be comparable to that of $KTiOPO_4$ (KTP, $d_{\text{eff}} \sim 3\,\text{pm V}^{-1}$) or ∼ ten times that of KDP in the IR region. It should be of note that in general an increase of bandgap would result in a decrease in the SHG coefficients (see section 2), and their balance needs to be evaluated in the search for and design of NLO materials.

Therefore, the three conditions of wide transmission window (large energy bandgap), moderate birefringence, and strong

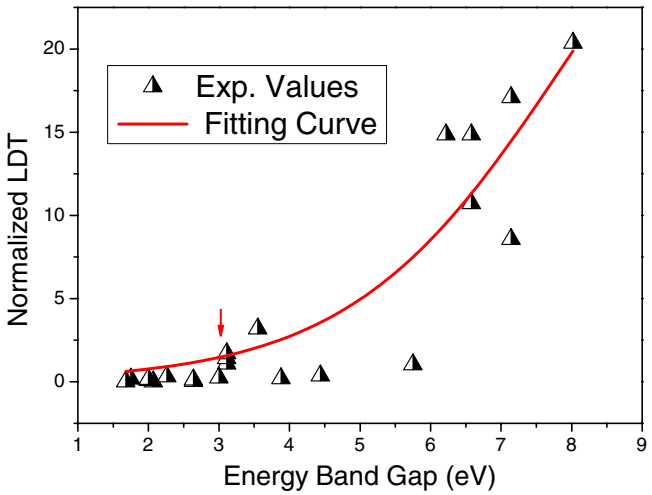

Figure 1. Tendency curve showing how the LDT and energy bandgap are related for the NLO crystals. The LDT is normalized to about 100 MW cm^{-2} for a nanosecond laser (indicated by a red arrow), which is enough for almost all academic and commercial purposes. Figures reprinted with permission from [48], Copyright 2013 The Royal Society of Chemistry.

SHG effects are commonly considered as basic for a good NLO material. In addition, good mechanical and chemical stabilities and easy growth habit are also very important for the practical applications of an NLO crystal [23].

Thorough elucidation of the structure–property relationship between NLO effects and microstructure is necessary for the exploration of new NLO crystals with good performance. It is indeed a very difficult task to discover a good NLO material from an enormous number of compounds just by the 'trial and error' method in experiments. Understanding of the mechanisms by which microscopic structures determine the macroscopic optical properties in materials will significantly enhance the searching efficiency. Quite a few theoretical models, such as Miller's rule [24], anharmonic oscillator models [25–27], the bond parameter and charge model [28, 29], the charge transfer model [30–32], and anionic group theory [33], have been proposed along with the discovery of various NLO materials. These models have successfully given intrinsic insight into the structure–property relation in specific types of crystals and greatly prompted the development of NLO materials. However, the calculations of SHG effects by these models were based on the empirical or semi-empirical approximate methods, which rely more or less on the experimental data.

Since the end of the 1990s, with the rapid development of computational methods and supercomputer facilities, the first-principles studies on the optical properties of crystals have been widely applied in the NLO materials [34–37]. The studies focus not only on the SHG coefficients, but also on other important optical parameters of NLO crystals, such as energy bandgap, refractive indices, and birefringence. The *ab initio* methods make it possible to predict the optical properties without any experimental data. Moreover, with the development of computational tools the microscopic mechanism for the linear and NLO properties can be explicitly deduced. These studies definitely have significant implications

for molecular engineering for the search for and design of good NLO crystals.

In this article, our first-principles studies on the NLO crystals are reviewed. In section 2 the applications of the density functional theory (DFT) to NLO crystals are presented. The development of first-principles methods and their application to the prediction and design of new NLO crystals are introduced in sections 3 and 4. Finally, the conclusion and future prospects for first-principles studies on NLO materials are given.

2. Applications of DFT to NLO crystals

DFT [38] is the most successful first-principles method to accurately predict the properties of materials [39], especially those determined by the electronic ground states. The optical properties, on the other hand, are usually determined by the electronic excited states, which is very difficult to deal with by DFT [40]. A most notorious case is the energy bandgap prediction; the local density approximation (LDA) [41] and generalized gradient approximation (GGA) [42] in the standard DFT usually underestimate the energy bandgaps, by even more than 40% for wide-gap insulators due to the discontinuity of exchange–correlation (XC) energy [43]. It is gratifying that various XC functionals beyond LDA and GGA have been developed, which have made substantial progress in solving this problem. These XC functionals commonly include HF (exact exchange, but no correlation), HF-LDA (exact exchange, plus LDA correction), sX (screened exchange, but no correlation), and sX-LDA (screened exchange, plus LDA correlation) forms [44], and hybrid functionals with B3LYP (combination of HF exchange with DFT XC) [45] and PBE0 (combination of Perdew–Burke–Ernzerhof (PBE) functional with a predefined amount of exact exchange) [46] forms. We have tested these XC functionals on many typical UV and IR NLO crystals. It was found that for the UV and deep-UV NLO crystals the calculated bandgaps with the hybrid B3LYP and PBE0 functionals are in very good agreement with experimental values (usually the relative error is less than 5%) [47], while for IR crystals the sX-LDA functionals can generally obtain satisfactory predictions [48]. These results actually demonstrate that the DFT calculations can give us a trustworthy way to predict the energy bandgap, which is very important for NLO materials engineering.

The linear and NLO properties of a material can be deduced by first-principles electronic band structure calculations. On the basis of the electronic structures, the imaginary part of the dielectric function ε_2 is calculated from the electronic transition between the occupied and unoccupied states caused by the interaction with photons [49]:

$$\varepsilon_2(\hbar\omega) = \frac{2\pi e^2}{\Omega\varepsilon_0}\sum_{k,v,c}\left|\langle\Psi_k^c|\hat{u}\cdot\vec{r}|\psi_k^v\rangle\right|^2\delta(E_k^c - E_k^v - \hbar\omega) \tag{2}$$

where Ω is the volume of the elementary cell, v and c represent the valence and conduction bands (CBs), respectively, ω is the frequency of the incident light, and $\hat{u}$ is the vector defining the polarization of the electric field of the incident light; $\left|\langle\Psi_k^c|\hat{u}\cdot\vec{r}|\Psi_k^v\rangle\right|$ under supercell geometry (periodic boundary conditions) can be expressed as the momentum matrix element between a CB and a valence band (VB) at a given k-point in the first Brillouin zone. Since the dielectric constant describes a causal response, the real and imaginary parts are linked by a Kramers–Kronig transform. Thus the real part of the dielectric function, $\varepsilon_1(\omega)$, and then the refractive index n and birefringence Δn, can be obtained.

The NLO properties of a crystal are mainly determined by the magnitudes of the static limit of the SHG coefficients $\chi^{(2)}(0)$, which plays the most important role in the applications of SHG crystals. Therefore, the formula originally proposed by Rashkeev *et al* [50] was adopted and improved, and the second-order susceptibility χ^{ijk} is represented as [51]

$$\chi^{ijk} = \chi^{ijk}(\mathrm{VE}) + \chi^{ijk}(\mathrm{VH}) + \chi^{ijk}\ (\text{two bands}) \tag{3}$$

where $\chi^{ijk}(\mathrm{VE})$ and $\chi^{ijk}(\mathrm{VH})$ denote the contributions from virtual-electron processes and virtual-hole processes, respectively, and χ^{ijk} (two bands) gives the contribution from two-band processes to $\chi^{(2)}$. The formulas for calculating $\chi^{ijk}(\mathrm{VE})$, $\chi^{ijk}(\mathrm{VH})$ and χ^{ijk} (two bands) are the following:

$$\chi^{ijk}(\mathrm{VE}) = \frac{e^3}{2\hbar^2 m^3}\sum_{\mathrm{vcc'}}\int\frac{\mathrm{d}^3\vec{k}}{4\pi^3}P(ijk)\mathrm{Im}[p^i_{\mathrm{vc}}p^j_{\mathrm{cc'}}p^k_{\mathrm{c'v}}] \times\left(\frac{1}{\omega^3_{\mathrm{cv}}\omega^2_{\mathrm{vc'}}} + \frac{2}{\omega^4_{\mathrm{vc}}\omega_{\mathrm{c'v}}}\right) \tag{3.1}$$

$$\chi^{ijk}(\mathrm{VH}) = \frac{e^3}{2\hbar^2 m^3}\sum_{\mathrm{vv'c}}\int\frac{\mathrm{d}^3\vec{k}}{4\pi^3}P(ijk)\mathrm{Im}[p^i_{\mathrm{vv'}}p^j_{\mathrm{v'c}}p^k_{\mathrm{cv}}] \times\left(\frac{1}{\omega^3_{\mathrm{cv}}\omega^2_{\mathrm{v'c}}} + \frac{2}{\omega^4_{\mathrm{vc}}\omega_{\mathrm{cv'}}}\right) \tag{3.2}$$

and

$$\chi^{ijk}(\text{two bands}) = \frac{e^3}{\hbar^2 m^3}\sum_{\mathrm{vc}}\int\frac{\mathrm{d}^3\vec{k}}{4\pi^3}P(ijk) \times\frac{\mathrm{Im}[p^i_{\mathrm{vc}}p^j_{\mathrm{cv}}(p^k_{\mathrm{vv}} - p^k_{\mathrm{cc}})]}{\omega^5_{\mathrm{vc}}}. \tag{3.3}$$

Here, i, j and k are Cartesian components, v and v′ denote VB, and c and c′ denote CB. $P(ijk)$ denotes full permutation. Past experience shows that this two-band term makes an extremely small contribution and can be neglected in any practical analysis; recently, it has been proven rigorously that the term is in fact precisely zero [52]. The band energy difference and momentum matrix elements between the electronic states m and n are denoted as $\hbar\omega_{mn}$ and p^α_{mn}, respectively, and they are all implicitly k-point (k) dependent. By this sum-over-states formula (3), the SHG coefficient component d_{ijk} (=1/2χ^{ijk}) is determined. Normally, d_{ijk} is abbreviated as d_{il} with the following subscript relationship between jk and l: 11 → 1; 22 → 2; 33 → 3; 23, 32 → 4; 13, 31 → 5; and 12, 21 → 6. It should be emphasized that the refractive indices and SHG coefficients can be accurately obtained by DFT in principle because these optical properties are determined by the virtual electronic excited processes which are described by the first- and second-order perturbations, respectively, on the ground state wavefunctions. Thus, the very precise electronic

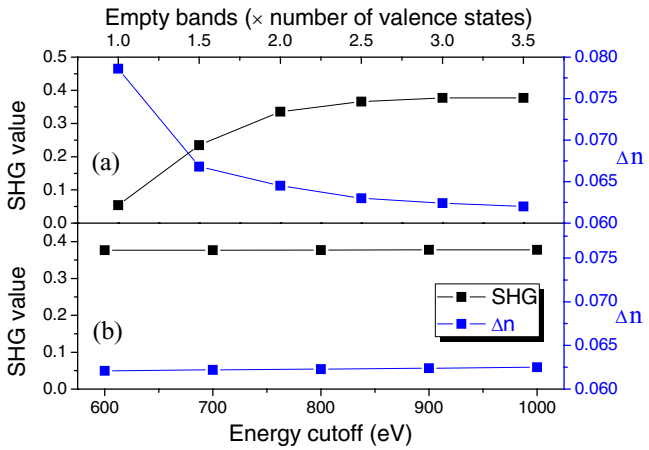

Figure 2. Convergence tests on the SHG coefficient and birefringence for KBBF with respect to (*a*) the number of empty bands and (*b*) the energy cutoff.

structure is necessary in order to accurately determine the optical properties of a crystal. For the strongly correlated systems containing transition or rare earth metals, however, it is still difficult to obtain the correct electronic properties without adjusting the parameters. The development of the relevant DFT methods is anticipated to overcome this problem.

Our further studies revealed that, although the energy bandgaps predicted by sX-LDA, B3LYP or PBE0 functionals are very accurate, the calculated linear and NLO properties are usually much smaller than the experimental data since the valence and CB widths are overestimated [47]. LDA or GGA, on the other hand, can well predict the optical properties by including a scissors operator [53] that shifts all the CBs to agree with the measured value of the bandgap. Therefore, the sX-LDA, B3LYP or PBE0 energy bandgap predictions combined with the scissors-corrected LDA or GGA calculations can provide an *ab initio* path to predict the refractive indices and SHG coefficients without introducing any experimental data.

In our DFT simulations the electronic structure calculations have been performed by the plane-wave pseudopotential method [54] implemented in the CASTEP package [55]. The qc-tuned optimized norm-conserving pseudopotentials [56] in the Kleinman–Bylander form [57] for the elements were usually used, which ensure a small plane-wave basis set without compromising the accuracy required by our study. Kinetic energy cutoffs of 900 eV and Monkhorst–Pack k-point meshes [58] spanning less than 0.04 $Å^{-3}$ in the Brillouin zone were typically chosen. For the optical properties the number of CBs was chosen as three times the number of VBs. Our trial results showed that the above computational parameters are sufficiently accurate for present purposes; an explicit example of the convergence tests for KBBF is shown in figure 2.

We have successfully applied the DFT method to many NLO crystals, ranging from UV and deep-UV borates to IR chalcogenides and halides, such as BBO (β-BaB_2O_4) [51], the LBO family (LiB_3O_5 (LBO), CsB_3O_5 (CBO) and $CsLiB_6O_{10}$ (CLBO)) [59], the KBBF family ($KBe_2BO_3F_2$ (KBBF), $RbBe_2BO_3F_2$ (RBBF) and $CsBe_2BO_3F_2$ (CBBF)) [60], the SBBO family ($Sr_2Be_2B2O_7$ (SBBO), $K_2Al_2B_2O_7$ (KABO), $BaAl_2B_2O_7$(BABO) and $BaAlBO_3F_2$ (BABF)) [61, 62], BiB_3O_6 (BIBO) [63], $YAl_3(BO_3)_4$ (YAB) [64], $AgGaX_2$ [65], $LiGaX_2$(X = S, Se or Te) [66], and $Cs_2HgI_2Cl_2$ [17]. The calculated linear and NLO coefficients are listed in tables 1 and 2, respectively, and exhibit a good agreement with the experimental values. This clearly demonstrates the validity of DFT theory for the NLO crystals. It is worth noting that recently semiconductor based NLO materials such as GaAs, AlGaAs, AlN and GaP have gained wide interest due to their compatibility with on-chip integration. In particular, some of these semiconductors are wide-band and can operate in the UV spectrum [67–69]. Similar DFT studies on these semiconductors have been performed [70].

3. Development of the first-principles studies on new NLO crystals

It is far from enough to just accurately predict the linear and NLO properties; elucidations of the structure–property relationship are more important for searching for and designing new NLO crystals with good performances. For this purpose we have developed several useful tools, including the real-space atom-cutting technique [51], SHG density scheme [64, 71], non-bonding state analysis and modified bond valence sum (MBVS) method [72]. All these tools have provided us with very efficient ways to investigate and understand the microscopic structural origins which determine the macroscopic optical properties in NLO crystals.

3.1. Real-space atom-cutting technique

The real-space atom-cutting technique [51] is used to analyze the contribution of the respective ions (or groups) to the optical properties. In this methodology, the real space is separated into individual zones (usually spheres), and each zone contains one ion. If the contribution to the overall optical properties of an ion (or a group) needs to be considered, the wavefunctions in the zones belonging to the other ions (or groups) are set to zero (which we refer to as 'atom-cutting'). In this way, the electronic transition elements involving the unconcerned ions (or groups) are removed and the contribution of the focusing ions (or group) is extracted. For instance, the contribution to the nth polarizability of group X is χ^n (X) = χ^n (all the atoms are cut except X). In the real-space atom-cutting method, the determination of cutting radii in general follows the rule that the radii should be contacting and not overlapping with each other.

We have adopted the real-space atom-cutting technique to study the microscopic structural origin of various NLO crystals. In the following subsection, some typical examples are given.

3.1.1. Borates containing the alkaline and/or alkaline earth A-site cations. The borates in which the A-site cations are alkaline and/or alkaline-earth cations usually transmit in the UV or even deep-UV spectral regions. So far almost all important UV and deep-UV NLO crystals are this type of borate (the only exception is KDP), e.g. BBO [73], the LBO family [74–77], the KBBF family [78–80] and the SBBO family [81–84]. In these crystals, the fundamental building

Table 1. Comparison of the experimental and calculated refractive indices and birefringence of (*a*) uniaxial and (*b*) biaxial NLO crystals.

	Experimental			Calculated		
(*a*)	n_o	n_e	Δn	n_o	n_e	Δn
BBO[a]	1.656	1.543	0.113	1.676	1.562	0.114
CLBO[b]	1.485	1.436	0.049	1.516	1.457	0.059
KBBF[c]	1.477	1.400	0.077	1.478	1.413	0.065
RBBF[c]	1.478	1.407	0.071	1.4883	1.4295	0.059
CBBF[c]	1.501	1.443	0.058	1.5126	1.4570	0.056
BABF[d]	1.619	1.557	0.042	1.6664	1.6227	0.044
BABO[e]	1.570	1.517	0.053	1.5757	1.5257	0.050
KABO[e]	1.560	1.492	0.068	1.559	1.5071	0.052
$LiGaTe_2$[f]	—	—	—	2.8101	2.8421	0.032
$AgGaS_2$[g]	2.4486	2.3954	0.0532	2.5840	2.5530	0.031
$AgGaSe_2$[g]	2.8932	2.8452	0.048	2.9798	2.9358	0.044
$AgGaTe_2$[g]	2.9859	3.0047	−0.0188	3.2678	3.2799	−0.0115
YAB[h]	1.7585	1.6881	0.070	1.7698	1.7011	0.0687

	Experimental				Calculated			
(*b*)	n_x	n_y	n_z	Δn	n_x	n_y	n_z	Δn
LBO[b]	1.566	1.590	1.607	0.041	1.585	1.599	1.632	0.047
CBO[b]	1.519	1.550	1.578	0.059	1.558	1.581	1.611	0.053
BIBO[i]	1.7585	1.7854	1.9190	0.1605	1.8391	1.7792	1.8717	0.0925
$LiGaS_2$[f]	2.0674	2.1048	2.1073	0.0399	2.1972	2.1403	2.14	0.0572
$LiGaSe_2$[f]	2.2373	2.2849	2.2882	0.0509	2.3356	2.3258	2.3423	0.0165

[a] Ref. [51].
[b] Ref. [59].
[c] Ref. [60].
[d] Ref. [62].
[e] Ref. [61].
[f] Ref. [66].
[g] Ref. [65].
[h] Ref. [64].
[i] Ref. [63].

Table 2. Experimental and calculated SHG coefficients in NLO crystals (unit: pm V^{-1}).

	Experimental	Calculated		Experimental	Calculated
BBO[a]	$d_{22} = \pm 1.60\ (1 \pm 0.05)$	$d_{22} = -1.38$	$LiGaS_2$[f]	$d_{31} = 5.8$	$d_{31} = -3.8$
	$d_{31} \leqslant (0.07 \pm 0.03) d_{22}$	$d_{31} = 0.056$		$d_{32} = 5.12$	$d_{32} = -3.1$
				$d_{33} = 10.7$	$d_{33} = 7.2$
LBO[b]	$d_{31} = \mp 0.98$	$d_{31} = -0.72$	$LiGaSe_2$[f]	$d_{31} = 10$	$d_{31} = -6.25$
	$d_{32} = \pm 1.05$	$d_{32} = 0.84$		$d_{32} = 7.7$	$d_{32} = -4.6$
	$d_{33} = \pm 0.059$	$d_{33} = -0.02$		$d_{33} = -18.2$	$d_{33} = 13.45$
CBO[b]	$d_{14} = \pm 0.75$	$d_{14} = -0.577$	$LiGaTe_2$[f]	$d_{31} = 42$	$d_{36} = -50.4$
CLBO[b]	$d_{36} = \pm 0.67$	$d_{36} = 0.546$	$AgGaS_2$[g]	$d_{36} = 11.0, 12.5$	$d_{36} = 14.1$
KBBF[c]	$d_{11} = 0.49$	$d_{11} = 0.41$	$AgGaSe_2$[g]	$d_{36} = 33$	$d_{36} = 45.2$
RBBF[c]	$d_{11} = 0.50$	$d_{11} = 0.40$	$AgGaTe_2$[g]	—	$d_{36} = 99.5$
CBBF[c]	$d_{11} = 0.50$	$d_{11} = 0.38$	YAB[h]	$d_{11} = 1.70$	$d_{11} = 1.657$
BABF[d]	$d_{22} = 1.10$	$d_{22} = 0.70$	BIBO[i]	$d_{22} = \pm 2.53$	$d_{22} = -2.95$
BABO[e]	$d_{11} = 0.75$	$d_{11} = 0.745$		$d_{16} = \pm 2.8$	$d_{16} = -2.55$
KABO[e]	$d_{11} = 0.45$	$d_{11} = -0.32$[j]		$d_{14} = \pm 2.4$	$d_{14} = -1.16$
KDP[j]	$d_{36} = 0.39$	$d_{36} = 0.42$		$d_{23} = \mp 1.3$	$d_{23} = -1.17$

[a] Ref. [51].
[b] Ref. [59].
[c] Ref. [60].
[d] Ref. [62].
[e] Ref. [61].
[f] Ref. [66].
[g] Ref. [65].
[h] Ref. [64].
[i] Ref. [63].
[j] Ref. [47].

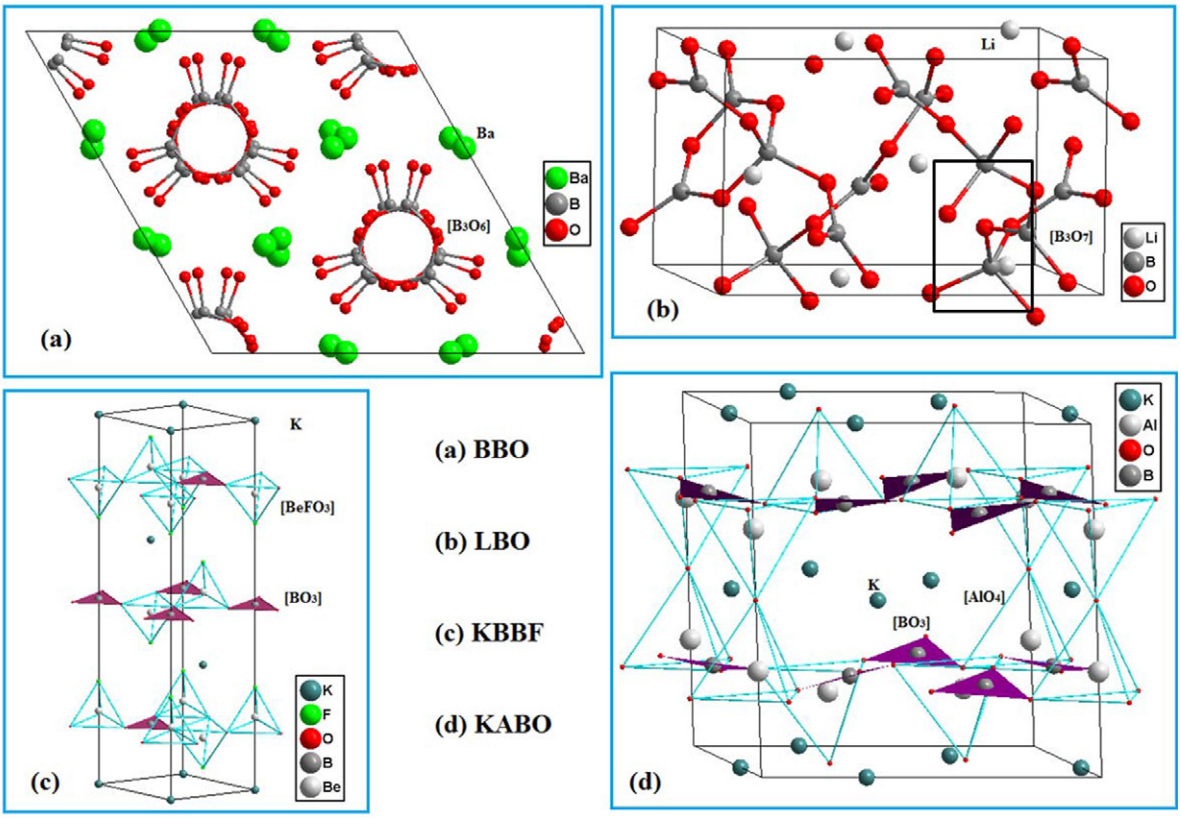

Figure 3. The crystal structure of (*a*) BBO, (*b*) LBO, (*c*) KBBF and (*d*) KABO.

blocks are composed of the B–O anionic groups, such as planar anionic $(B_3O_6)^{3-}$ rings (figure 3(*a*)), continuous networks of $(B_3O_7)^{5-}$ groups (figure 3(*b*)), and $(BO_3)^{3-}$triangles interconnected by BeO_3F or AlO_4 tetrahedra (figures 3(*c*) and (*d*)), while the A-site alkaline and/or alkaline earth cations are located in the interstices. The real-space atom-cutting analyses for these crystals are listed in table 3, and several conclusions can be deduced, as follows. (i) Although the *A-site* cations (especially for Rb^+, Cs^+, Sr^{2+}, and Ba^{2+}) have considerable contribution to the refractive index, even comparable to that of the B–O anionic groups, they almost contribute nothing to the optical birefringence due to their strong iconicity. (ii) The birefringence is mainly contributed by the B–O groups, such as $(B_3O_6)^{3-}$ in BBO, $(B_3O_7)^{5-}$ in the LBO family, and $(BO_3)^{3-}$ in the KBBF family and SBBO family. (iii) The contribution from the A-site cations to the SHG coefficients increases as their radius increases. For instance, the Li^+ ions only contribute 1% to the largest component d_{32} in LBO, while for CBO the contribution of the Cs^+ ions to d_{14} is around 15%. However, these A-site cations contribute no more than 20% to the overall SHG effects. (iv) The anionic groups predominantly determine the magnitude of SHG coefficients in the UV and deep-UV borate crystals. In BBO and the LBO family $(B_3O_6)^{3-}$ and $(B_3O_7)^{5-}$ contribute more than 80% to the largest SHG coefficients, while in the KBBF family and SBBO family the combined contribution from $(BO_3)^{3-}$ and other anionic groups such as $(BeO_3F)^{4-}$ in the KBBF family and $(BeO_4)^{5-}$ or $(AlO_4)^{5-}$ in the SBBO family accounts for more than 75% of the overall SHG effects. The above observations originate from the fact that the sphere-like shape of the A-site cations is almost optical isotropic and the responses of conjugated π orbitals in the anionic groups to the incident light are strongly anisotropic. Our real-space atom-cutting results confirm and support the conclusions from the anionic group theory [33]: i.e., the microscopic second-order susceptibilities of the B–O anionic groups determine the macroscopic SHG coefficients in the UV and deep-UV NLO borates.

3.1.2. BIBO and YAB. One may ask if the conclusion that the B–O groups determine SHG effects in borates is valid, as the A-site cations are not alkaline or alkaline earth cations. To investigate this point in depth, two borates, BiB_3O_6 (BIBO) [85, 86] and $YAl_3(BO_3)_4$ (YAB) [87] with 'the A-cations' Bi and Y, respectively, were chosen to perform the atomic level analysis. In BIBO the BO_3 triangles and BO_4 tetrahedra in a ratio of 2 : 1 are linked by the four-coordinated bismuth cations to form a three-dimensional hinge structure (figure 4(*a*)), while in YAB the coplanar BO_3 triangles are connected with the Al^{3+} cations to construct a network with the linkage of six-coordinated Y cations (figure 4(*b*)). Detailed first-principles electronic structure calculations revealed that the charge densities around both Bi and Y cations are not spherical but form significant covalent chemical bonds with the neighbour O anions, establishing the $(BiO_4)^{4-}$ quadrangular pyramids [63] and deformed $(YO_6)^{9-}$ octahedra [64], respectively.

The real-space atom-cutting results for BIBO and YAB are listed in table 4, from which some conclusions can be

Table 3. Calculated and experimental values of the optical properties and the contributions of the respective groups in BBO, the LBO family, the KBBF family, and the SBBO family.

BBO	n_o	n_e	$\Delta n\ (n_o - n_e)$	d_{22}	d_{31}	d_{33}	
$(B_3O_6)^{3-}$	1.5280	1.4114	0.1166	−1.50	−0.039	−0.030	
Ba^+	1.2396	1.2392	0.0004	−0.36	−0.059	0.045	
Total	1.6851	1.5695	0.1156	−1.86	−0.098	0.015	
Experimental	1.69267	1.66736	0.12471	$\pm 1.60\ (1 \pm 0.05)$	∼0	∼0	
LBO	n_x	n_y	n_z	$\Delta n(n_{max} - n_{min})$	d_{31}	d_{32}	d_{33}
$(B_3O_7)^{5-}$	1.564	1.578	1.607	0.043	−0.496	0.571	−0.008
Li^+	1.048	1.052	1.051	0.004	−0.008	0.002	−0.034
Total	1.557	1.575	1.605	0.045	−0.505	0.582	−0.044
Experimental	1.566	1.591	1.606	0.041	±0.67	±0.85	±0.04
CBO	n_x	n_y	n_z	$\Delta n(n_{max} - n_{min})$	d_{14}		
$(B_3O_7)^{5-}$	1.360	1.373	1.414	0.054	−0.342		
Cs^+	1.279	1.280	1.285	0.006	−0.098		
Total	1.557	1.575	1.605	0.048	−0.577		
Experimental	1.519	1.551	1.578	0.059	±1.04		
CLBO	n_o	n_e	$\Delta n\ (n_o - n_e)$	d_{36}			
$(B_3O_7)^{5-}$	1.419	1.357	0.062	−0.222			
Li^+	1.0290	1.0287	0.0003	−0.006			
Cs^+	1.125	1.124	0.001	−0.138			
Total	1.513	1.455	0.058	−0.546			
Experimental	1.485	1.436	0.049	±0.95			
KBBF	n_o	n_e	$\Delta n\ (n_o - n_e)$	d_{11}			
$(BO_3)^{3-}$	1.3183	1.2242	0.094	0.376			
$(BeO_3F)^{5-}$	1.3088	1.2626	0.046	0.113			
K^+	1.0874	1.0879	−0.0005	0.014			
Total	1.4694	1.4069	0.063	0.41			
Experimental	1.477	1.400	0.077	0.49			
RBBF	n_o	n_e	$\Delta n\ (n_o - n_e)$	d_{11}			
$(BO_3)^{3-}$	1.3551	1.2766	0.079	0.369			
$(BeO_3F)^{5-}$	1.3458	1.3113	0.035	0.126			
Rb^+	1.1884	1.1928	−0.0044	0.030			
Total	1.4883	1.4295	0.059	0.40			
Experimental	1.478	1.407	0.071	0.50			
CBBF	n_o	n_e	$\Delta n\ (n_o - n_e)$	d_{11}			
$(BO_3)^{3-}$	1.4221	1.3607	0.061	0.124			
$(BeO_3F)^{5-}$	1.3690	1.3371	0.032	0.359			
Cs^+	1.4532	1.4270	0.026	0.128			
Total	1.5126	1.4570	0.056	0.38			
Experimental	1.501	1.443	0.058	0.50			
BABO	n_o	n_e	$\Delta n\ (n_o - n_e)$	d_{11}			
$(BO_3)^{3-}$	1.3423	1.2711	0.071	0.348			
$(AlO_4)^{5-}$	1.3876	1.3818	0.006	0.267			
Ba^{2+}	1.1616	1.1492	0.012	0.115			
Total	1.5757	1.5257	0.050	0.75			
Experimental	1.698	1.636	0.062	0.745			
KABO	n_o	n_e	$\Delta n\ (n_o - n_e)$	d_{11}			
$(BO_3)^{3-}$	1.311	1.256	0.055	−0.152			
$(AlO_4)^{5-}$	1.367	1.349	0.018	−0.283			
K^+	1.125	1.124	0.001	−0.012			
Total	1.527	1.478	0.049	−0.425			
Experimental	1.560	1.492	0.068	−0.317			
BABF	n_o	n_e	$\Delta n\ (n_o - n_e)$	d_{22}			
$(BO_3)^{3-}$	1.4490	1.3799	0.0691	0.323			
$(AlF_2O_3)^{5-}$	1.5081	1.4899	0.0182	0.233			
Ba^{2+}	1.2612	1.2507	0.0105	0.092			
Total	1.7698	1.7152	0.0546	0.702			
Experimental	1.619	1.557	0.042	1.10			

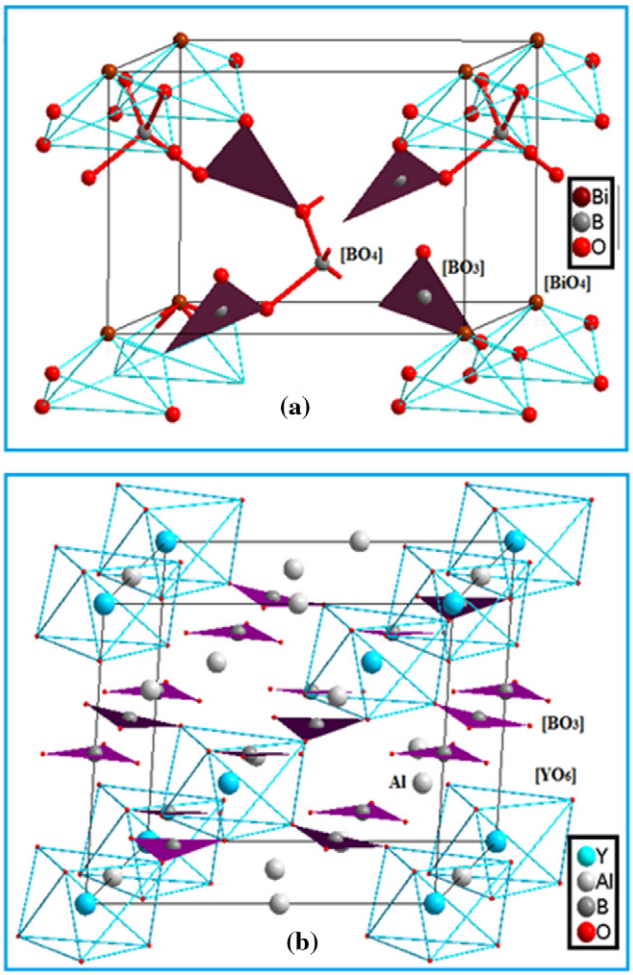

Figure 4. The crystal structure of (*a*) BIBO and (*b*) YAB.

deduced: (i) In BIBO the birefringence mainly originates from the coplanar $(BO_3)^{3-}$ groups as in the case of section 3.1.1. However, the anionic $(BiO_4)^{4-}$ group contributes more than 90% to the two large SHG coefficients d_{22} and d_{16}. This means that the NLO response in this crystal predominantly stems from the $(BiO_4)^{4-}$ group rather than from B–O anionic groups. This is because the $(BiO_4)^{5-}$ groups are distorted tetragons and the bismuth cations carry the parallel oriented lone-pair electrons, which results in a much greater contribution to the SHG effects compared with the $(BO_3)^{3-}$ group. (ii) In YAB, the Al^{3+} ions almost contribute nothing to both the linear and NLO properties. The $(BO_3)^{3-}$ group contributes more than 90% to the birefringence, but its contribution to the NLO effect is much smaller than that of the $(YO_6)^{9-}$ group, which exceeds 80% in the overall SHG coefficients. The detailed structural analysis shows that the $(YO_6)^{9-}$ group is heavily distorted from the regular octahedron and the resulting second-order Jahn–Teller effect [88] causes large microscopic second-order susceptibilities, similar to the (NbO_6) and (TiO_6) groups in $LiNbO_3$ and $BaTiO_3$, respectively [89, 90]. The real-space atom-cutting technique, therefore, clarifies that the NLO effect in these crystals does not mainly originate from the B–O anionic groups, and the contribution from the Bi–O or Y–O groups is even more important.

3.1.3. $LiGaX_2$ and $AgGaX_2$ (X = S, Se or Te). We further investigated the origins of linear and NLO properties in $LiGaX_2$ [91, 92] and $AgGaX_2$ (X = S, Se or Te [93–95]), two series of important IR NLO crystals, using the real-space atom-cutting technique. In both crystal families, all gallium atoms are four coordinated with X atoms and the lithium (or silver) cations are embedded in the cavities formed by the GaX_4 tetrahedra (see figure 5). It is interesting that the $LiGaX_2$ crystals have larger energy bandgaps and birefringence but smaller SHG coefficients compared with the $AgGaX_2$ crystals.

The atom-cutting analysis (see table 5) reveals that the Li^+ cations contribute almost nothing to the refractive indices, while the contribution of Ag^+ cations is considerable. On the other hand, the linear optical anisotropy, i.e. the birefringence, is predominantly determined by the GaX_4 tetrahedra and the contribution from the Li or Ag cations is negligibly small, mainly due to the fact that the Ga–X chemical bonds are much more covalent than the Li–X (or Ag–X) bonds. This conclusion is also available for the NLO effect: i.e., the Ga–X groups contribute much more than the Li or Ag cations to the SHG coefficients.

The electronic structural calculations show that in $LiGaX_2$ the outer-shell electronic orbitals on Li cations contribute almost nothing to the VB, while in $AgGaX_2$ quite a few Ag d orbitals are located at the top of the VB and raise the energy level of the VB maximum, resulting in the narrower energy bandgaps in the latter crystals [65, 66]. Since the SHG coefficients are approximately inversely proportional to the fifth power of the energy bandgap (see formula (3)), the SHG effect in $LiGaX_2$ is smaller than that in $AgGaX_2$. In addition, the larger birefringence in the $LiGaX_2$ compared with $AgGaX_2$ is because the GaX_4 groups in the former are more deformed from the regular tetrahedral shape compared with those in the latter, although the Li cations contribute less than the Ag cations to birefringence.

3.2. SHG density analysis

Through the atom-cutting technique, one can quantitatively obtain the contribution of the respective ions or groups to the linear and NLO properties in the crystals. In order to more intuitively identify the orbitals that contribute to the SHG effect in the real space, we developed a SHG-weighted charge density analysis tool [64, 71]. In this method, the considered SHG coefficient is 'decomposed' onto the respective orbital or band according to a 'band-resolved' scheme [96], and then the SHG-weighted bands are used to sum the charge densities of all occupied or unoccupied states. Thus, the electronic states irrelevant to SHG are not shown in the occupied or unoccupied 'SHG densities', and the orbitals vital to SHG are highlighted in real space.

Figure 6 displays the charge density and SHG density on the plane of the B_3O_6 group in BBO. It is clearly demonstrated that, although there are considerable charge densities present around the Ba cations, their SHG densities are much smaller than those on the B_3O_6 groups. The SHG effects in BBO are mainly contributed by the oxygen 2p orbitals with a figure-of-eight shape and the nonlocal orbitals in the B_3O_6 groups, consistent with the real-space atom-cutting results.

Table 4. Calculated and experimental values of the optical properties and the contributions of the respective groups in BIBO and YAB.

BIBO	n_x	n_y	n_z	Δn	d_{22} (pm V^{-1})	d_{16} (pm V^{-1})	d_{14} (pm V^{-1})	d_{23} (pm V^{-1})
Experimental	1.7585	1.7854	1.9190	0.1605	±2.53	±2.8	±2.4	∓1.3
Origin	1.8391	1.7792	1.8717	0.0925	−2.95	−2.55	−1.16	−1.17
$(BO_3)^{3-}$	1.5514	1.5242	1.5991	0.0749	−0.233	−0.628	0.372	0.243
$(BO_4)^{5-}$	1.4014	1.3782	1.4240	0.0458	−0.118	−0.334	0.391	0.050
$(BiO_4)^{5-}$	1.6922	1.6388	1.6746	0.0534	−2.829	−2.090	−1.412	−1.182
YAB	n_e	n_o	Δn	d_{11} (pm V^{-1})				
Experimental	1.6881	1.7585	0.070	1.70				
Origin	1.7011	1.7698	0.0687	1.657				
Al^{3+}	1.0483	1.0525	0.0042	−0.001				
$(BO_3)^{3-}$	1.3666	1.4362	0.0696	0.685				
$(YO_6)^{9+}$	1.4290	1.4385	0.0095	1.421				

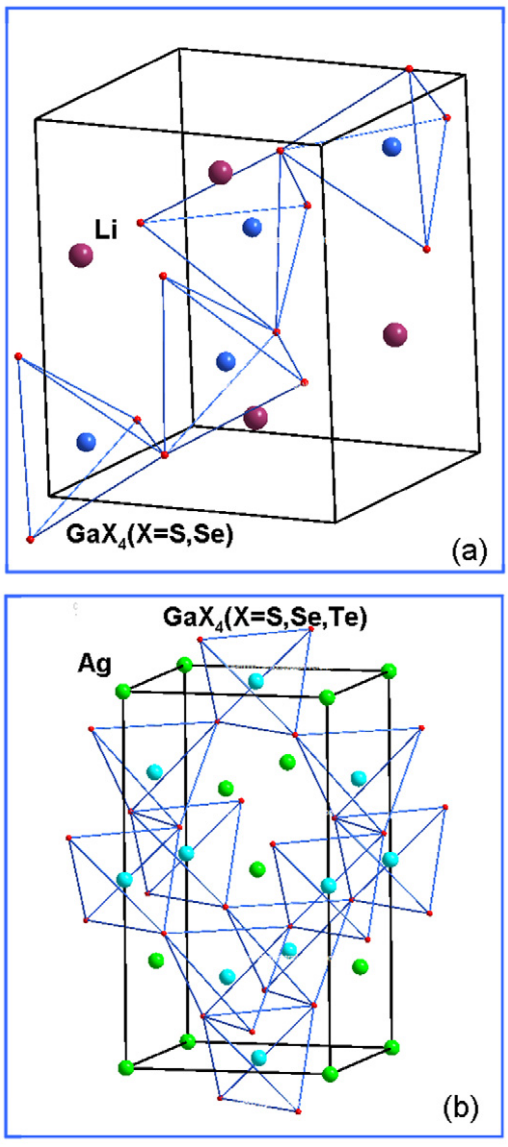

Figure 5. The unit cell of (*a*) $LiGaX_2$ and (*b*) $AgGaX_2$.

The SHG densities on the BO_3 and Y-Al planes in YAB are shown in figure 7, which reveals that the orbitals on both the BO_3 groups and the Y cations (or the Y–O groups) have significant contribution to the SHG effect, while the contribution from the Al^{3+} cations should be negligibly small. This is also confirmed by the atom-cutting method (see table 4), where the contribution of $(YO_6)^{9-}$ groups (1.42 pm V^{-1}) to the SHG coefficient d_{11} is very large, even larger than that of $(BO_3)^{3-}$ groups (0.68 pm V^{-1}).

Therefore, it is concluded that the SHG density analysis provides a visualized tool to directly identify the orbitals on which ions or groups contribute to NLO properties and further to investigate in depth the intrinsic origins of the SHG effect in crystals.

3.3. Non-bonding state analysis and MVBS method

As mentioned above, apart from the SHG coefficients and birefringence, the energy bandgap (or short wavelength cutoff) is a key factor to determine the application range of an NLO crystal. Therefore, accurate prediction of the energy bandgap is vital for the discovery of new NLO crystals with good performance. However, it is usually very difficult to grow crystals with high optical quality in experiments so as to accurately measure the energy bandgap at the initial stage of materials discovery. On the other hand, the DFT methods with the LDA and GGA XC functionals seriously underestimate the energy bandgap (see section 2). Recent attempts have been devoted to solving this problem by using the higher level XC functionals such as the GW approximation, exact exchange [97], hybrid and screened-hybrid functionals (e.g. PBE0 and B3LYP) [98], time-dependent DFT [99], and the Δ-sol method [100], but these methods are quite computational resource consuming and only simple unitary and binary semiconductors were considered in these studies. Therefore, it is necessary to develop a rapid and effective method to predict the bandgap in NLO crystals.

We focus on the energy bandgap prediction in the borates which transmit a wavelength less than 200 nm (corresponding to the energy bandgap $E_g > 6.2$ eV) due to their very important NLO applications in the UV and deep-UV spectral regions. Based on the DFT electronic structure calculations with PBE0 XC functionals which have the ability to predict the energy bandgap with high precision [47], we have analyzed the electronic states that determine the energy bandgap and proposed a very effective empirical method, i.e. the MBVS method, to accurately predict the energy bandgaps in the UV borates.

Table 5. Calculated and experimental values of the optical properties and the contributions of the respective groups in $LiGaX_2$ and $AgGaX_2$ (X = S, Se, and Te) crystals.

$LiGaS_2$		$Li+$	GaS_2^-	Origin	Experimental
	n_x	1.1234	2.1798	2.1972	2.0674
	n_y	1.1226	2.1250	2.1403	2.1048
	n_z	1.1181	2.1224	2.1400	2.1073
	Δn	0.0053	0.0574	0.0572	0.0572
	d_{31} (pm V^{-1})	0.0	−3.80	−3.80	−5.80
	d_{32} (pm V^{-1})	0.0	−3.10	−3.10	−5.12
	d_{33} (pm V^{-1})	0.0	7.01	7.20	10.7
$LiGaSe_2$		Li^+	$GaSe_2^-$	Origin	Experimental
	n_x	1.1274	2.3190	2.3356	2.2373
	n_y	1.1268	2.3112	2.3258	2.2849
	n_z	1.1258	2.3257	2.3423	2.2882
	Δn	0.0015	−0.0145	0.0165	0.0509
	d_{31} (pm V^{-1})	0.0	−6.25	−6.25	10.0
	d_{32} (pm V^{-1})	0.0	−4.55	−4.60	7.7
	d_{33} (pm V^{-1})	0.0	13.05	13.45	−18.20
$LiGaTe_2$		Li^+	$GaTe_2^-$	Origin	Experimental
	n_o	1.4611	2.7901	2.8101	—
	n_e	1.4504	2.8264	2.8421	—
	Δn	0.0107	−0.0363	0.0320	—
	d_{36} (pm V^{-1})	−0.70	−49.55	−50.40	−42
$AgGaS_2$		Ag^+	GaS_2^-	Origin	Experimental
	n_o	1.4373	2.3503	2.5840	2.4486
	n_e	1.4341	2.3364	2.5530	2.3954
	Δn	0.0032	0.0139	0.031	0.0532
	d_{36} (pm V^{-1})	0.52	14.84	14.10	11.0, 12.5
$AgGaSe_2$		Ag^+	$GaSe_2^-$	Origin	Experimental
	n_o	1.4676	2.7355	2.9798	2.8932
	n_e	1.4630	2.7275	2.9358	2.8452
	Δn	0.0040	0.0080	0.0440	0.048
	d_{36} (pm V^{-1})	1.18	46.25	45.20	33
$AgGaTe_2$		Ag^+	$GaTe_2^-$	Origin	Experimental
	n_o	1.4442	3.0090	3.2678	2.9859
	n_e	1.4497	3.0541	3.2799	3.0047
	Δn	−0.0055	−0.0451	−0.0115	−0.0188
	d_{36} (pm V^{-1})	2.22	90.0	99.5	—

Four representative borate UV NLO crystals, BBO, LBO, KBBF, and BABF, have been chosen for the DFT electronic structure calculations, and the partial densities of states (PDOSs) close to the forbidden band projected on the constituent atoms are shown in figure 8. The PDOSs clearly exhibit the strong hybridization between B and O orbitals in the upper region of the VB, indicating their strong covalent chemical bonds. More importantly, the energy range close to the VB maximum is exclusively occupied by O 2p orbitals and these electronic states have negligibly small hybridization with any other orbitals, so forming non-bonding states or dangling bonds. Accordingly, we introduce a parameter R_{NB}, defined as the ratio of the focused orbital total density of state (DOS) at a given energy level, and the orbitals with $R_{NB} > 0.9$ are considered as the non-bonding orbitals [101]. Using this parameter the non-bonding orbitals in the electron structures are quantitatively identified, shown in the shaded areas in figure 9. If these non-bonding states are eliminated, all energy bandgaps of these crystals would approach about 9.0 eV. In the other words, the energy bandgap in the UV borates is determined by the non-bonding states.

Figure 10 exhibits the charge densities of these non-bonding states projected on real space in the four borate crystals. Indeed the non-bonding states are located at the oxygen atoms, but their magnitude strongly depends on the local chemical environment around the oxygen atoms. Thus, we slightly modified the bond valence sum method, named as the MBVS method [72], to characterize these local environments. In the MBVS method, the modified bond valence of an oxygen atom is defined by the sum of the bond valences of the bonds connected to the atom:

$$V_M = \sum_i \exp\left(\frac{R_0 - R_i}{b}\right) \tag{4}$$

where R_i is the bond length between the central oxygen atom and the ith surrounding atom in a real crystal, R_0 is a tabulated parameter, expressing the ideal bond length when the ith atom contributes exactly unit valence to the central atom, and b is an empirical constant representing the variation of bond valence with respect to bond length (typically 0.37 Å for borates) [102].

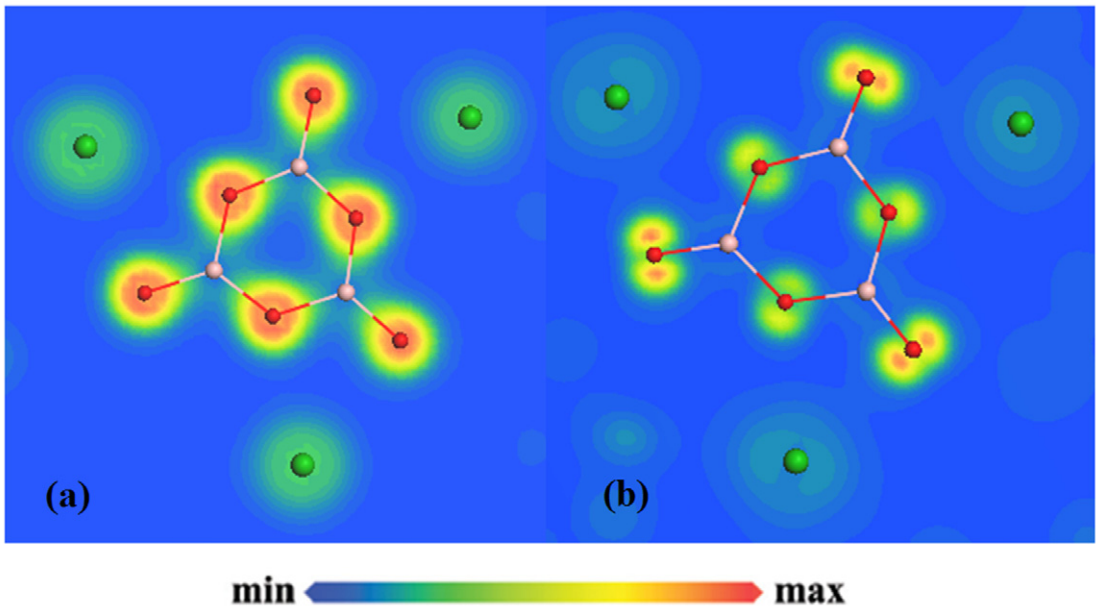

Figure 6. (a) Charge density and (b) SHG density on the plane of the (B_3O_6) group in BBO.

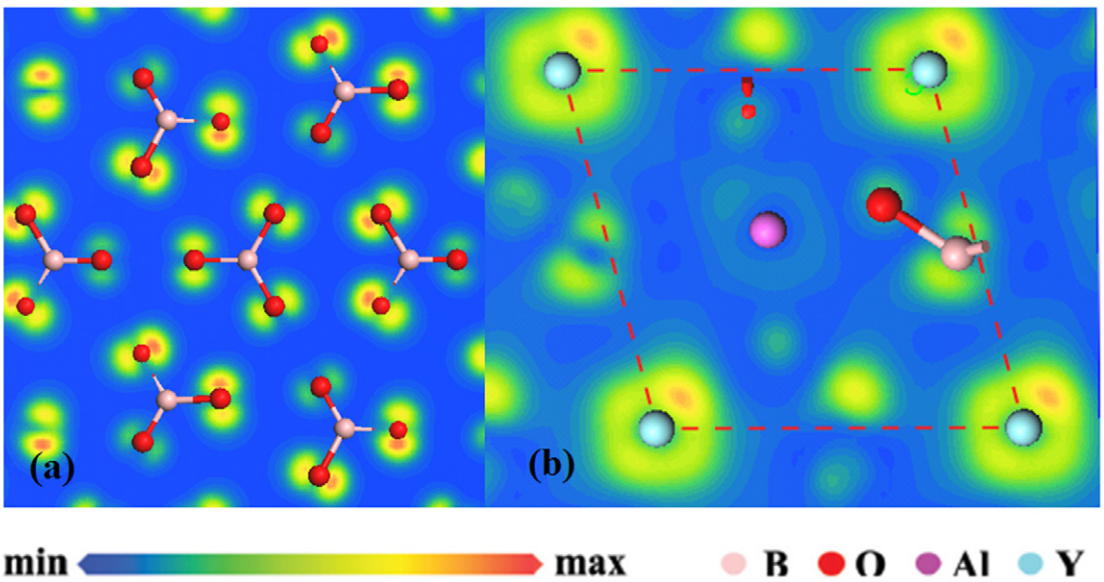

Figure 7. SHG densities on the (a) (BO_3) groups and (b) Y-Al planes in YAB. Figures reprinted with permission from [64], Copyright 2011 American Institute of Physics.

Here we only account for the contribution from the neighbour B-site cations, since the interactions between the A-site cations and oxygen anions have no influence on the non-bonding states. Clearly, the larger the V_M is, the fewer non-bonding electrons remain on the oxygen. Thus, the smallest $V_M(V_M\,(\min))$ identifies the highest number of the non-bonding orbitals on oxygen atoms and determines the bandgap in a UV borate.

Figure 11(a) displays the bandgap E_g as a function of V_M (min) in several representative UV borates, which shows a very strong linear dependence. Their relationship can be fitted by the least square method as

$$E_g = 1.83V_M(\min) + 4.41. \quad (5)$$

To verify the generalization of the MBVS method, formula (5) is used to predict the bandgaps of all UV borates whose experimental values have been determined accurately. The results shown in Figure 11(b) clearly demonstrate a very good agreement between the predicted and experimental values with the relative error less than 5%. It should be emphasized that our studies ignore the UV borates in which the B–O units are BO_4 groups exclusively; for these crystals formula (5) should be re-fitted.

In summary, the non-bonding state analysis based on the DFT electronic structure calculations provides understanding of the origins of the energy bandgap difference in UV borates, and the MBVS method further offers an effective way to predict their energy bandgaps based on the structural features.

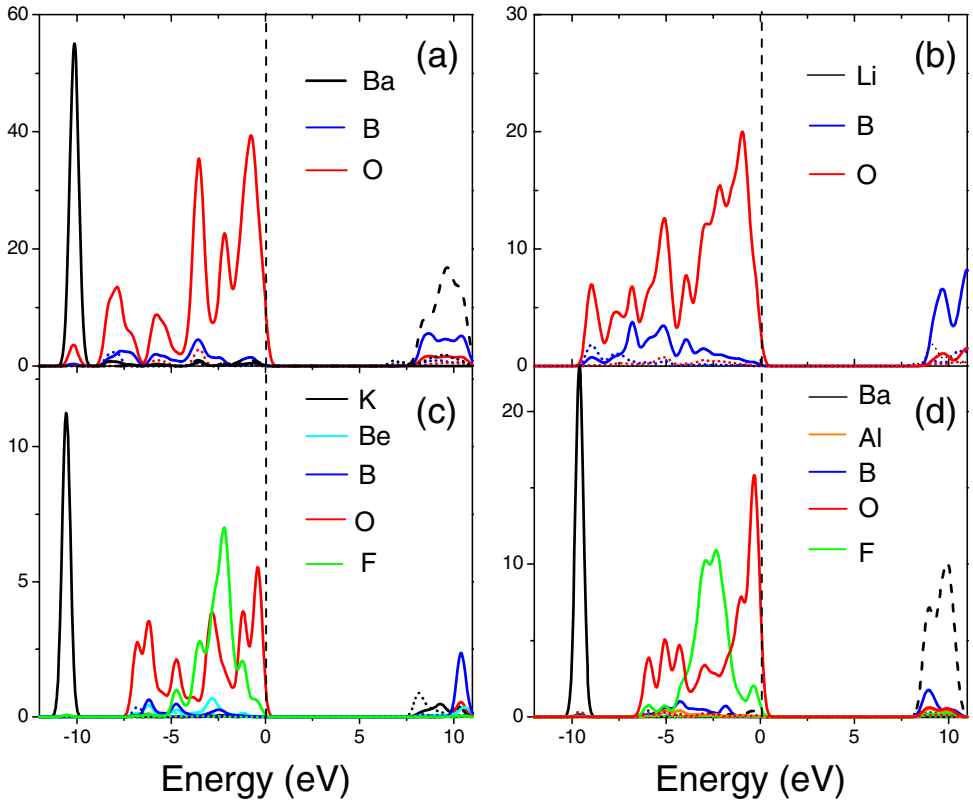

Figure 8. PDOS of (*a*) BBO, (*b*) LBO, (*c*) KBBF, and (*d*) BABF. Figures reprinted with permission from [101], Copyright 2011 Institute of Physics.

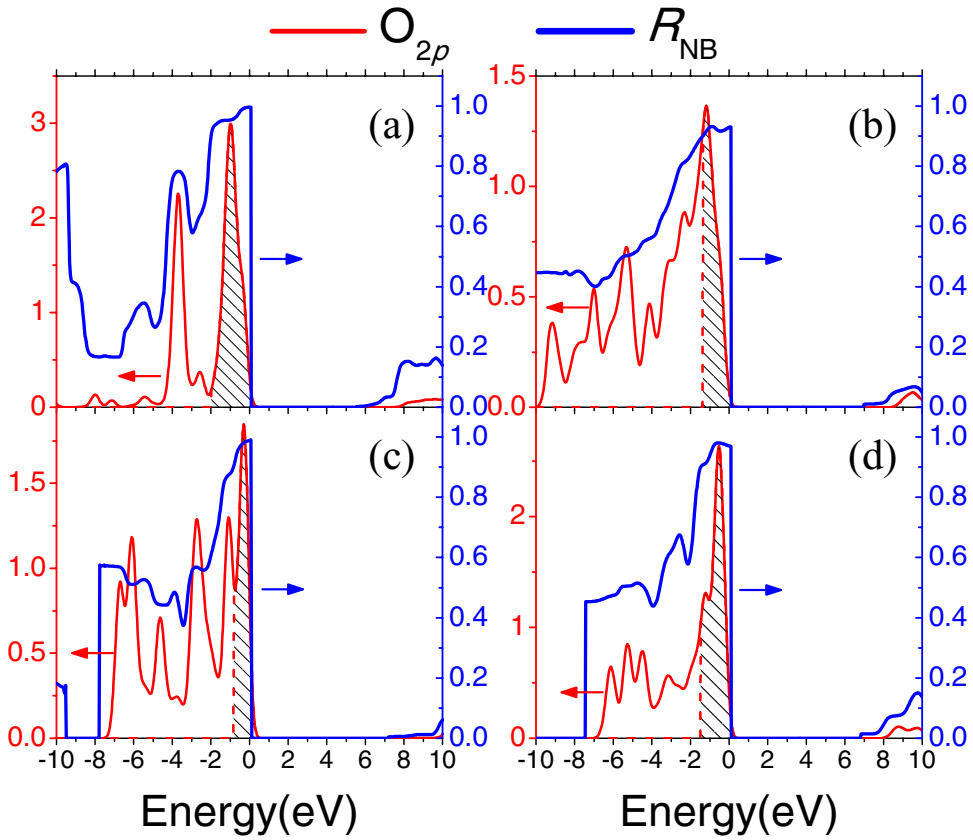

Figure 9. PDOS of the O 2p orbitals and the corresponding R_{NB} curves for (*a*) BBO, (*b*) LBO, (*c*) KBBF and (*d*) BABF. The shadow parts indicate the non-bonding orbitals. Figures reprinted with permission from [101], Copyright 2011 Institute of Physics.

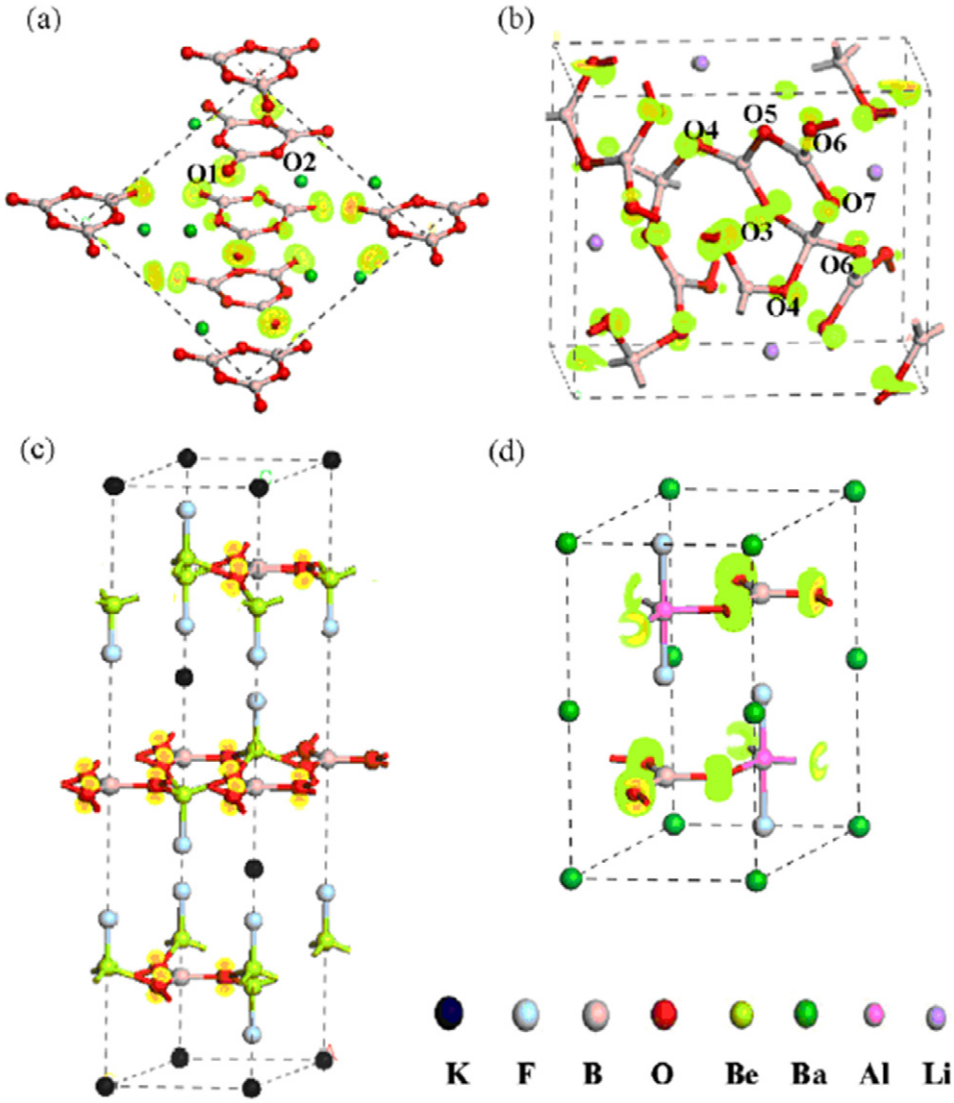

Figure 10. The charge densities of these non-bonding states projected on the real space in (*a*) BBO, (*b*) LBO, (*c*) KBBF, and (*d*) BABF. Figures reprinted with permission from [101], Copyright 2011 Institute of Physics.

4. First-principles prediction and design

In the above sections, first-principles methods have been adopted to investigate the intrinsic origins of the linear and NLO properties in NLO crystals from the microscopic scale. Understanding of the structure–property relationship can lead us to develop a molecular engineering method for the design of new NLO materials in experiments. In this section the materials applications for the prediction and design of new NLO crystals by DFT are exemplified.

4.1. Molecular engineering on new UV borates

Here $MM'Be_2B_2O_6F$ (M = Na, M′ = Ca; M = K, M′ = Ca, Sr) [103] and $LaBeB_3O_7$ [104] are presented as two representative examples. The structure of $MM'Be_2B_2O_6F$ was deduced from that of SBBO, which contains $(Be_6B_6O_{15})_\infty$ layers with parallel BO_3 arrangement favourable to achieve good NLO properties. However, SBBO has a serious structural polymorphism problem due to the large size of Sr^{2+} cations located between the layers and the relatively short Be–O bond lengths connecting the neighbouring layers, as revealed by the first-principles analysis [61, 105]. Thus, we considered using F^- anions to substitute the bridged O^{2-} anions between the layers in the SBBO structure. This is because the Be−F bond length is larger than that of the Be−O bond, and this would make the space between the adjacent layers more flexible. Thus, the Be atoms are more 'comfortably' accommodated at their original sites, which may decrease the occurrence of stacking faults in the SBBO-type crystal. Meanwhile, the alkaline cations such as Na^+, K^+, and Ca^+ cations are introduced into the SBBO structure to partially or totally substitute Sr^{2+} cations for charge balance. As a result, the series of new UV borates $MM'Be_2B_2O_6F$ (M = Na, M′ = Ca; M = K, M′ = Ca, Sr) were successfully synthesized in experiments through this molecular engineering design. It was proven that the new structural features

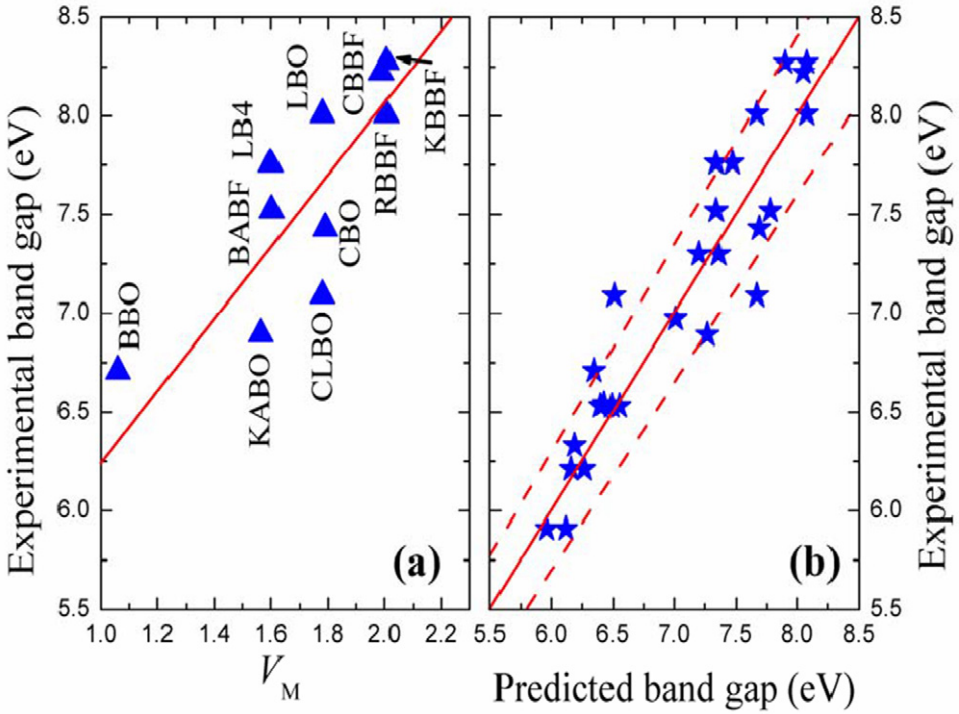

Figure 11. (*a*) Relationship between the V_M(min) parameters and the energy gaps in the representative UV borates. The straight line is fitted from formula (5). (*b*) Experimental bandgaps versus MBVS predicted values. The dashed lines indicate the relative error boundaries of ±5%. Figures reprinted with permission from [72], Copyright 2013 American Institute of Physics.

overcome the polymorphism problem inherent in the SBBO structure [103].

$LaBeB_3O_7$ was deduced from SrB_4O_7 (SBO), a NLO borate with very low UV absorption edge (~130 nm). The microscopic units accounting for the optical anisotropy in SBO are the tetrahedral BO_4 anionic groups, which have birefringence too small to achieve the phase-matching condition. In order to overcome this problem, we introduced the Be^{2+} cations into the SBO structure to partly replace the B^{3+} cations by forming the $(BO_4)^{5-}$ and $(BeO_4)^{6-}$ anionic groups in a molar ratio of 0.5:0.5. Although both anionic groups have relatively small birefringence [33, 106], the deformation of the local environments around the BO_4 and BeO_4 groups can result in the enhancement of the overall anisotropy. At the same time, the La^{3+} cations were chosen to substitute the Sr^{2+} cations due to their close ionic radius. By this molecular engineering design, the new $LaBeB_3O_7$ compound was discovered, which exhibits good phase-matching capabilities at the wavelength of 1064 nm [104].

4.2. Prospect evaluation of the deep-UV NLO carbonate crystals

For a long time, borates have been considered as the only candidates for the deep-UV NLO crystals. Recently, Ye's group has discovered several fluoride carbonates, i.e., the $MNCO_3F$ (M = K, Rb, Cs; N = Ca, Sr, Ba) family [16], which exhibits promising potential as NLO crystals in the deep-UV region. However, due to the limits of crystal growth it is very difficult to obtain large crystals with high quality and to thoroughly perform the experimental evaluations in the current stage. The first-principles calculations, thus, provide an effective and accurate way to investigate the prospects of these NLO crystals in the UV and deep-UV regions.

In particular, the fluoride carbonates with the formula $A_l(CO_3)_kF_m$ (A represents the alkaline and/or alkaline-earth metal elements) invoke our specific interest because they usually have very large energy bandgap and relatively large NLO effect. We have explored all carbonates with the $A_l(CO_3)_kF_m$ formula in the Inorganic Crystal Structural Database [107] and catalogued them into three classes according to their structural features, as shown in figure 12. In figures 12(*a*) and (*b*) the triangle planar $(CO_3)^{2-}$ groups are both flat lying with the orientation exactly parallel in the former and partly antiparallel in the latter, while in figure 12(*c*) the $(CO_3)^{2-}$ groups are standing on edge with respect to the overall structural layering. Our first-principles linear and NLO properties are in good agreement with the available experimental results, demonstrating the validity of our first-principles methods on the carbonate NLO crystals [108]. The detailed comparison with the UV NLO borates reveals that the fluoride carbonates with the flat-lying structures have larger birefringence ($\Delta n > 0.1$) than that of UV borates ($\Delta n \sim 0.07$), and they are suitable to be birefringent crystals which can be used for polarizers, beam displacers and beam splitters in the UV region. Moreover, these carbonates have a stronger SHG effect than do UV borates, so they are very good candidates for the harmonic generation of 266 nm coherent light, which has important applications in industry, but the

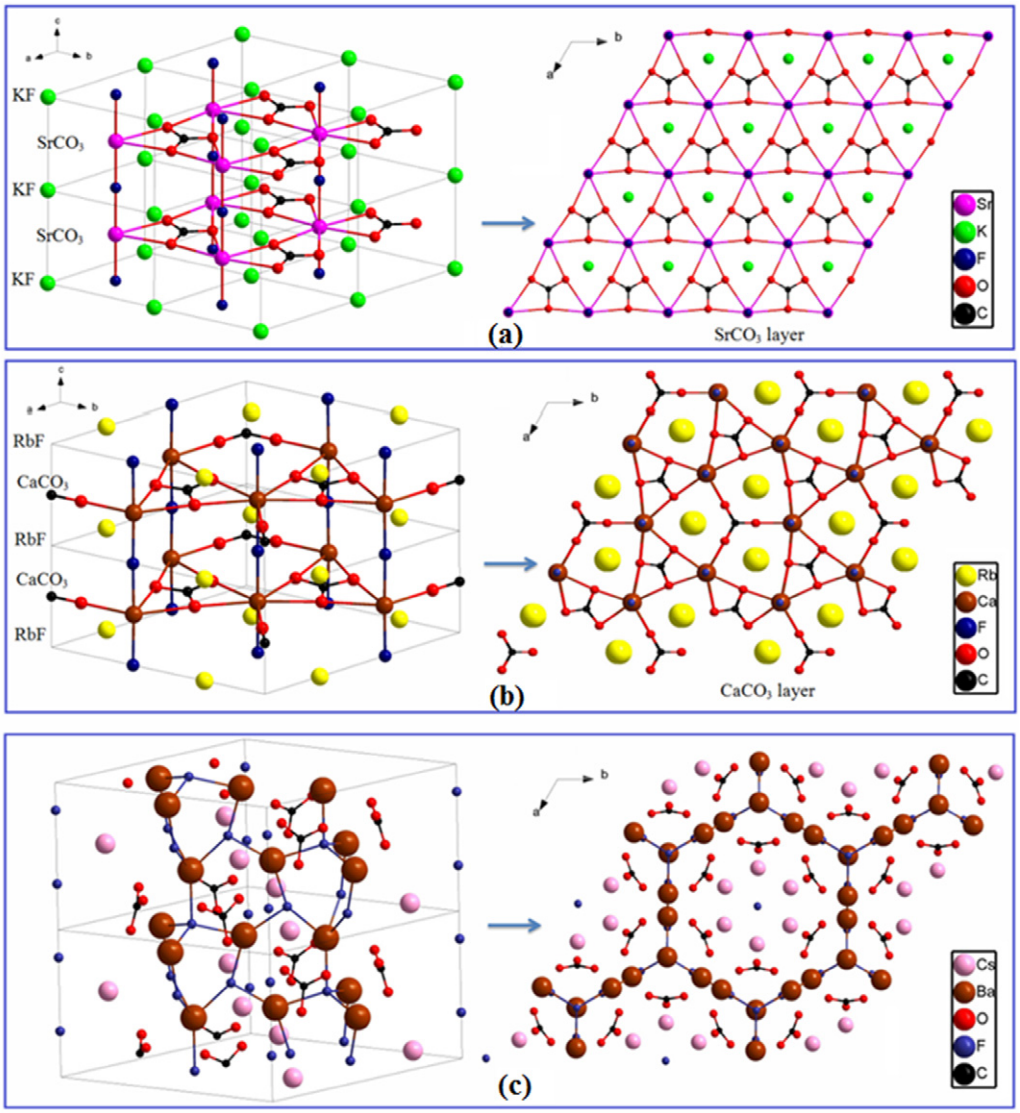

Figure 12. Crystal structures in the UV fluoride carbonates according to their structural features: (*a*) the triangle planar (CO_3) groups are flat lying with the orientation exactly parallel, (*b*) the (CO_3) groups are flat lying but partly antiparallel, (*c*) the (CO_3) groups are standing on edge with respect to the overall structural layering. Figures reprinted with permission from [108], Copyright 2013 American Chemical Society.

available NLO crystals are still in great demand. However, it should be emphasized that the energy bandgaps of all known fluoride carbonates are less than 6.3 eV (wavelength > 195 nm), which is not large enough for deep-UV harmonic generation. As comparison, the UV borates BABF and KBBF possess much shorter UV edges of 165 nm and 150 nm, respectively.

In order to investigate if it is possible to find the fluoride carbonates with large energy bandgaps, the non-bonding state analysis presented in section 3.3 has been performed in the known $A_l(CO_3)_kF_m$ crystals. As shown in figure 13, similar to the case of UV borates the O 2p non-bonding states are located at the VB maximum and determine the energy bandgap in the fluoride carbonates. The elimination of these non-bonding states can be fulfilled by modifying the local chemical environment around the oxygen atoms. With the guidance of this idea, we consider that the incorporation of lightweight metal cations from groups IIA and IIIA could improve the energy bandgaps in carbonates [108].

Through systematically substituting Ca^{2+}, Sr^{2+} or Ba^{2+} cations by Be^{2+} or Al^{3+} atoms in $MNCO_3F$, we theoretically discovered two novel fluoride carbonates, $KBeCO_3F$ and $RbAlCO_3F_2$ [109], which are kinetically stable (i.e. have a phonon spectrum without imaginary vibration frequency), and their structures are plotted in figure 14. Our first-principles calculations predict that both $KBeCO_3F$ and $RbAlCO_3F_2$ possess very large energy bandgaps, 7.61 eV (~164 nm) and 8.21 eV (~152 nm), respectively. Meanwhile, their birefringence and SHG coefficients are larger than those in KBBF. The excellent linear and NLO properties in $KBeCO_3F$ and $RbAlCO_3F_2$ demonstrate that both crystals have very good deep-UV SHG capabilities comparable to those of KBBF. Upon being obtained, these crystals would be applied as excellent deep-UV NLO materials.

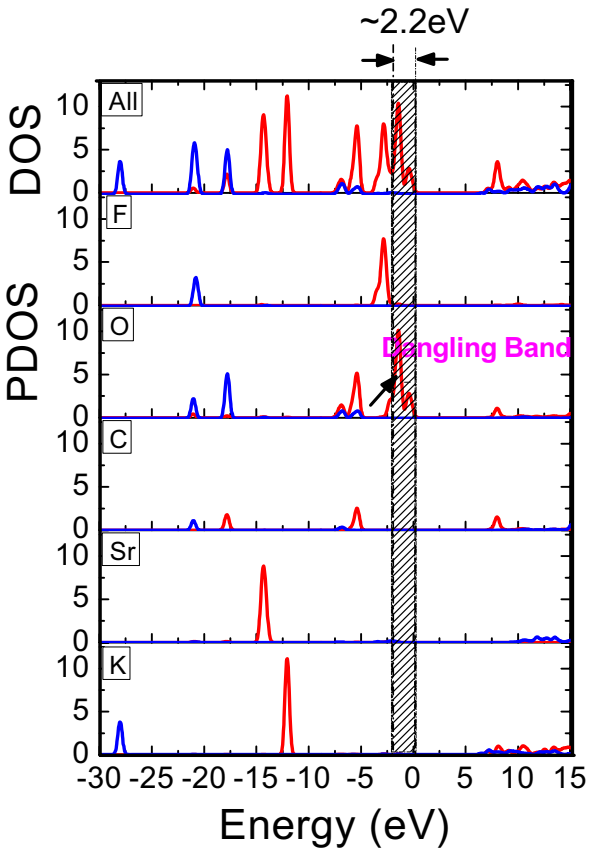

Figure 13. PDOS in a UV fluoride carbonate. The non-bonding states are indicated by the shaded areas.

4.3. Selection and design of mid-IR NLO halide crystals

Low LDT is one of the major barriers in the practical applications of the commercially used mid-IR NLO crystals including $AgGaS_2$ [110], $AgGaSe_2$ [111], $ZnGeP_2$ [112], and $LiBC_2$ (B = Al, Ga, In; C = S, Se, Te) [91, 113]. It is known that the LDT is closely relevant to the energy bandgap (E_g) in crystals, but an increase of bandgap usually results in a decrease in the SHG effect. Thus, the key issue in the search for and design of good mid-IR NLO materials is to achieve a balance between having a large bandgap and strong SHG effects. In general, it is required that a good mid-IR NLO material should have an energy bandgap larger than 3.0 eV (corresponding to about 100 MW cm^{-2} for a nanosecond laser, see figure 1) and SHG effects larger than 10(d_{eff} of KDP), which are enough for almost all academic and commercial purposes.

The halide-based materials attract our interest since they exhibit wide IR transmission, reasonable SHG coefficients and relatively high LDT [114–119]. However, systematic investigation of the structural selections of the mid-IR halide materials with good NLO performances is still lacking. The first-principles studies, hence, give insight into structure–property relations for the linear and NLO properties of mid-IR NLO halides at the atomic level. We classify the halide crystals into four types according to their fundamental structural units [MX_k], where M is the central metal cation, X is the halide anion and k = 6, 4, 3, 2, i.e. [MX_6] distorted octahedra, [MX_4] tetrahedra, [MX_3] triangular pyramids and [MX_2] one-dimensional strings (see figure 15). To comprehensively understand the influence of the halogen ions on the optical properties, we also construct a series of hypothetical halide crystals by substituting one type of halogen ion with another in some known halides.

Figure 16 displays the distribution of energy bandgaps with respect to the SHG effect in all the crystals studied. It is clear that the increase of energy bandgap E_g is usually accompanied by a decrease of SHG coefficients d_{ij}, confirming that it is indeed a key issue to seek a balance between E_g and d_{ij} for finding good NLO mid-IR halides. In general, the fluorides possess large energy bandgap but small SHG effect, while the iodides possess large SHG effect but small energy bandgap, so neither of them are suitable candidates for mid-IR NLO applications. The halide crystals which satisfy the requirement for being a good mid-IR NLO crystal, i.e. bandgap greater than 3.0 eV and SHG effect larger than 10 × KDP (as shown by the yellow region in figure 16), are the chlorides and bromides containing [MX_4], [MX_3] or [MX_2] units [48]. It is convincing that this atomic level insight based on the DFT calculations will be significant in the search for and design of new wide-gap NLO crystals with large SHG effect in the mid-IR spectral region.

5. Conclusion and future prospects

NLO crystals are very important to development of laser technology and related scientific fields. Explorations of new NLO crystals with good performances in various spectral regions are of perpetual interest in optoelectronic functional materials. Unlike many technological applications, where it is very hard to find properties at the microscopic scale, NLO materials are a good field for first-principles predictions since the key optical properties, including birefringence, SHG coefficients, and even energy bandgaps, can be readily obtained from the atomic level. It should be emphasized that, besides the applications presented in this review, the DFT methods can also be used to study other properties in the NLO crystals, such as the crystal stability [105] and the influence of impurities or defects on the optical properties in crystals [120–123]. Therefore, first-principles simulations, as the third research method apart from pure theoretical and experimental investigations, can significantly prompt the discovery of NLO crystals. Namely, the *ab initio* calculations can be employed to judge if it is desired to perform further single-crystal growth for precise optical measures at the initial stage of a new compound discovery. Moreover, elucidation of the structure–property relations and the structural selections deduced from the first-principles simulations would guide the explorations of good NLO materials in experiments. It is anticipated that the first-principles studies not only significantly improve the search efficiency, e.g. shorten the exploration period from about 15 years [3, 124] on average to less than 6 years, but also greatly help experiments to save huge human and raw material resources. In fact, this computer-based molecular-engineering research approach is consistent with the essence of the Materials Genome Initiative [125] currently proposed

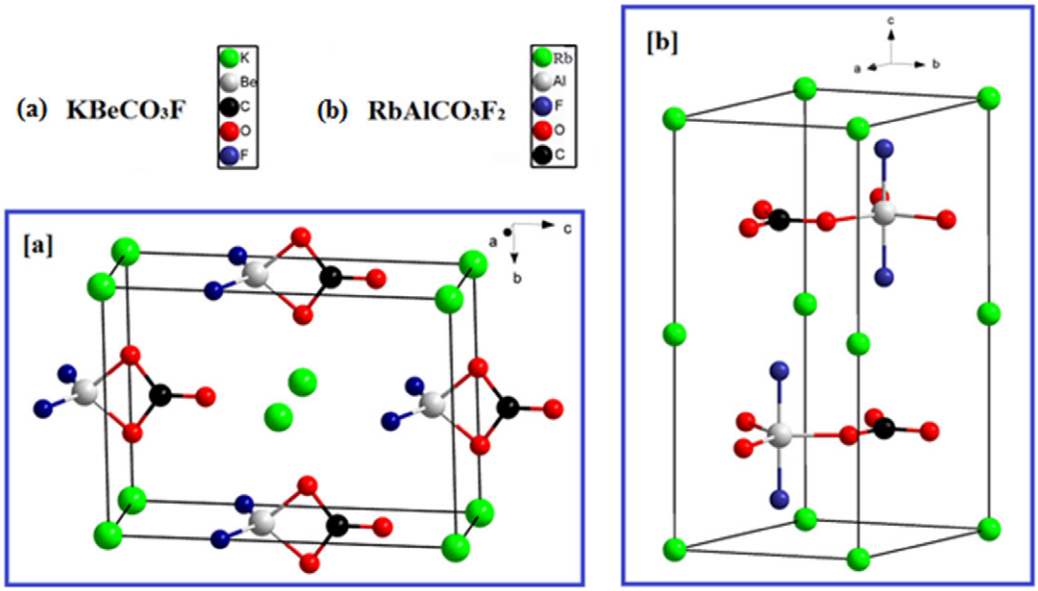

Figure 14. Unit cell of (a) $KBeCO_3F$ and (b) $RbAlCO_3F_2$. Figures reprinted with permission from [109], Copyright 2013 Nature.

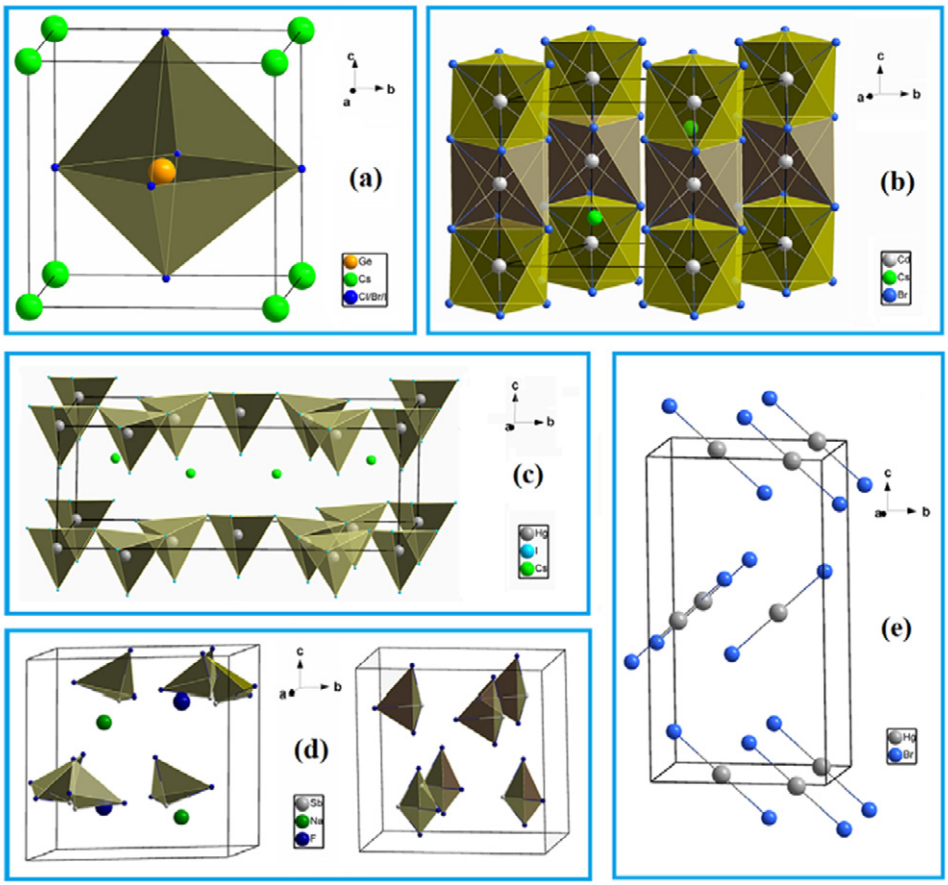

Figure 15. Structures of IR NLO halides according to their fundamental structural units. [MX_k] units in (a, b) [MX_6] distorted octahedra, (c) [MX_4] tetrahedra, (d) [MX_3] triangular pyramids and (e) [MX_2] one-dimensional strings. Figures reprinted with permission from [48], Copyright 2013 The Royal Society of Chemistry.

by the White House in the USA. We believe that first-principles studies will play more and more important roles in the discovery of new functional materials, not merely of NLO crystals.

Acknowledgments

This work was supported by the National Natural Science Foundation of China under grant Nos 11174297 and 91022036,

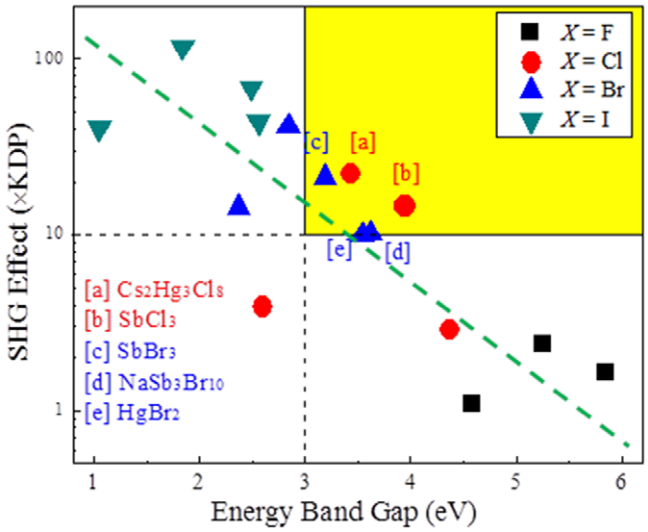

Figure 16. Bandgap distribution as a function of the SHG effect for all the halides studied. It is clear that the SHG effect decreases as the energy bandgap increases in these crystals as indicated by the dashed straight line obtained by least square fitting. The shaded area represents the region where good mid-IR NLO crystals are expected. Figures reprinted with permission from [48], Copyright 2013 The Royal Society of Chemistry.

and the National Basic Research Project of China (Nos 2010CB630701 and 2011CB922204).

References

[1] Franken P A, Weinreich G, Peters C W and Hill A E 1961 *Phys. Rev. Lett.* **7** 118–9
[2] Savage N 2007 *Nature Photon.* **1** 83–5
[3] Cyranoaki D 2009 *Nature* **457** 953–5
[4] Xu Y M *et al* 2011 *Nature Phys.* **7** 198–202
[5] Zhang W T *et al* 2008 *Phys. Rev. Lett.* **100** 107002–5
[6] Chai B H T 1995 Optical crystal *CRC Handbook of Laser Science and Technology, Supplement 2: Optical Materials* ed M J Weber (Boca Raton, FL: CRC Press) pp 3–65
[7] Burland D M, Miller R D and Walsh C A 1994 *Chem. Rev.* **94** 31–75
[8] Jundt D 2009 Nonlinear optical crystals for use in consumer laser projection displays (IEEE Photonics Society Santa Calra Valley Chapter)
[9] Lin X, Zhang G and Ye N 2009 *Cryst. Growth Des.* **9** 1186–9
[10] Zhang G, Qin J G, Liu T, Li Y J, Wu Y C and Chen C T 2009 *Appl. Phys. Lett.* **95** 261104
[11] Bera T K, Jang J I, Song J H, Malliakas C D, Freeman A J, Ketterson J B and Kanatzidis M G 2010 *J. Am. Chem. Soc.* **132** 3484–95
[12] Wang S, Ye N, Li W and Zhao D 2010 *J. Am. Chem. Soc.* **132** 8779–86
[13] Zhang W L, Cheng W D, Zhang H, Geng L, Lin C S and He Z Z 2010 *J. Am. Chem. Soc.* **132** 1508–9
[14] Huang H, Yao J, Lin Z, Wang X, He R, Yao W, Zhai N and Chen C 2011 *Angew. Chem. Int. Edn Engl.* **50** 9141–4
[15] Wang S C and Ye N 2011 *J. Am. Chem. Soc.* **133** 11458–61
[16] Zou G, Ye N, Huang L and Lin X 2011 *J. Am. Chem. Soc.* **133** 20001–7
[17] Zhang G *et al* 2012 *J. Am. Chem. Soc.* **134** 14818–22
[18] Boyd R W 2008 *Nonlinear Optics* (New York: Academic)
[19] Zondy J J 1998 *Opt. Commun.* **149** 181–206
[20] Fejer M M, Magel G A, Jundt D H and Byer R L 1992 *IEEE J. Quantum Electron.* **28** 2631–54
[21] Baudrier-Raybaut M, Haidar R, Kupecek P, Lemasson P and Rosencher E 2004 *Nature* **432** 374–6
[22] Zhang X, Wang L, Wang X, Wang G, Zhu Y and Chen C 2012 *Opt. Commun.* **285** 4519–22
[23] Chen C T, Ye N, Lin J, Jiang J, Zeng W R and Wu B C 1999 *Adv. Mater.* **11** 1071–8
[24] Miller R C 1964 *Appl. Phys. Lett.* **5** 17–9
[25] Kurtz S K and Robinson F N H 1967 *Appl. Phys. Lett.* **10** 62–5
[26] Garrett C G B and Robinson F N H 1966 *IEEE J. Quantum Electron.* **QE-2** 328–9
[27] Garrett C G B 1968 *IEEE J. Quantum Electron.* **QE-4** 70–84
[28] Jeggo C R and Boyd G D 1970 *J. Appl. Phys.* **41** 2741–3
[29] Bergman J G and Crane G R 1974 *J. Chem. Phys.* **60** 2470–4
[30] Levine B F 1969 *Phys. Rev. Lett.* **22** 787–90
[31] Levine B F 1970 *Phys. Rev. Lett.* **25** 440–3
[32] Levine B F 1973 *Phys. Rev.* B **7** 2600–26
[33] Chen C T 1993 Development of new NLO crystals in the borate series *Laser Science and Technology, An International Handbook* vol 15, ed V S Letokhov *et al* (Chur, Switzerland: Harwood) chapter 1
[34] Chen C, Lin Z and Wang Z 2005 *Appl. Phys.* B **80** 1–25
[35] Huang Y Z, Wu L M, Wu X T, Li L H, Chen L and Zhang Y F 2010 *J. Am. Chem. Soc.* **132** 12788–9
[36] Kong F, Huang S P, Sun Z M, Mao J G and Cheng W D 2006 *J. Am. Chem. Soc.* **128** 7750–1
[37] Wu H P, Yu H W, Yang Z H, Hou X L, Su X and Pan S L 2013 *J. Am. Chem. Soc.* **135** 4215–8
[38] Kohn W 1999 *Rev. Mod. Phys.* **71** 1253–66
[39] Martin R M 2005 *Electronic Structure: Basic Theory and Practical Methods* (Cambridge: Cambridge University)
[40] Tozer D J, Amos R D, Handy N C, Roos B O and Serrano-Andres L 1999 *Mol. Phys.* **97** 859–68
[41] Kohn W and Sham L J 1965 *Phys. Rev.* **140** A1133–8
[42] Perdew J P and Wang Y 1986 *Phys. Rev.* B **33** 8800–2
[43] Wang C S and Klein B M 1981 *Phys. Rev.* B **24** 3417–29
[44] Seidl A, Gorling A, Vogl P, Majewski J A and Levy M 1996 *Phys. Rev.* B **53** 3764–74
[45] Becke A D 1993 *J. Chem. Phys.* **98** 5648–52
[46] Ernzerhof M and Scuseria G E 1999 *J. Chem. Phys.* **110** 5029–36
[47] Lin Z S, Kang L, Zheng T, He R, Huang H and Chen C T 2012 *Comput. Mater. Sci.* **60** 99–104
[48] Kang L, Ramo D M, Lin Z S, Bristowe P D, Qin J G and Chen C T 2013 *J. Mater. Chem.* C **1** 7363–70
[49] Palik E D 1985 *Handbook of Optical Constants of Solids* (New York: Academic)
[50] Rashkeev S N, Lambrecht W R L and Segall B 1998 *Phys. Rev.* B **57** 3905–19
[51] Lin J, Lee M H, Liu Z P, Chen C T and Pickard C J 1999 *Phys. Rev.* B **60** 13380–9
[52] Li C S and Lee M H 2010 Methodology of calculating NLO properties of materials: improving a SHG code and implementing a THG code *Master Degree Thesis* Tamkang University
[53] Godby R W, Schluter M and Sham L J 1988 *Phys. Rev.* B **37** 10159–75
[54] Payne M C, Teter M P, Allan D C, Arias T A and Joannopoulos J D 1992 *Rev. Mod. Phys.* **64** 1045–97
[55] Clark S J, Segall M D, Pickard C J, Hasnip P J, Probert M J, Refson K and Payne M C 2005 *Z. Kristallogr.* **220** 567–70
[56] Lee M H, Lin J S, Payne M C, Heine V, Milman V and Crampin S 2005 Ψ_k *Newsletters* **67** (February) Highlights
[57] Kleinman L and Bylander D M 1982 *Phys. Rev. Lett.* **48** 1425–8
[58] Monkhorst H J and Pack J D 1976 *Phys. Rev.* B **13** 5188–92
[59] Lin Z S, Lin J, Wang Z Z, Chen C T and Lee M H 2000 *Phys. Rev.* B **62** 1757–64

[60] Kang L, Luo S, Huang H, Zheng T, Lin Z S and Chen C T 2012 *J. Phys.: Condens. Matter* **24** 335503
[61] Lin Z S, Wang Z Z, Chen C T, Chen S K Y and Lee M H 2003 *J. Appl. Phys.* **93** 9717–23
[62] Huang H, Lin Z S, Bai L, Hu Z G and Chen C T 2009 *J. Appl. Phys.* **106** 103107
[63] Lin Z S, Wang Z Z, Chen C T and Lee M H 2001 *J. Appl. Phys.* **90** 5585–90
[64] He R, Lin Z S, Lee M H and Chen C T 2011 *J. Appl. Phys.* **109** 103510
[65] Bai L, Lin Z S, Wang Z Z, Chen C T and Lee M H 2004 *J. Chem. Phys.* **120** 8772–8
[66] Bai L, Lin Z S, Wang Z Z and Chen C T 2008 *J. Appl. Phys.* **103** 083111
[67] Xiong C, Pernice W, Sun X K, Schuck C, Fong K Y and Tang H X 2012 *New J. Phys.* **14** 095014
[68] Xiong C, Pernice W, Ryu K, Schuck C, Fong K, Palacios T and Tang H X 2011 *Opt. Express* **19** 10464–70
[69] Rivoire K, Lin Z L, Hatami F, Masselink T and Vuckovic J 2009 *Opt. Express* **17** 22609–15
[70] Hughes L P, Wang Y and Sipe J E 1997 *Phys. Rev.* B **55** 13630–40
[71] Lo C H and Lee M H 2004 The role of electron lone-pair in the optical nonlinearity of oxide, nitride and halide crystals *Master Degree Thesis* Tamkang University
[72] He R, Huang H W, Kang L, Yao W J, Jiang X X, Lin Z S, Qin J G and Chen C T 2013 *Appl. Phys. Lett.* **102** 231904
[73] Chen C T, Wu B C, Jiang A D and You G M 1985 *Sci. Sin.* B **28** 235–43
[74] Chen C T, Wu Y C, Jiang A D, You G M, Li R K and Lin S J 1989 *J. Opt. Soc. Am.* B **6** 616–21
[75] Wu Y C, Sasaki T, Nakai S, Yokotani A, Tang H G and Chen C T 1993 *Appl. Phys. Lett.* **62** 2614–5
[76] Mori Y, Kuroda I, Nakajima S, Sasaki T and Nakai S 1995 *Appl. Phys. Lett.* **67** 1818–20
[77] Tu J M and Keszler D A 1995 *Mater. Res. Bull.* **30** 209–15
[78] Chen C T, Wang Y B, Xia Y N, Wu B C, Tang O Y, Wu K, Zeng W and Yu L H 1995 *J. Appl. Phys.* **77** 2268–72
[79] Chen C T, Luo S Y, Wang X Y, Wang G L, Wen X H, Wu H X, Zhang X and Xu Z Y 2009 *J. Opt. Soc. Am.* B **26** 1519–25
[80] Huang H, Chen C, Wang X, Zhu Y, Wang G, Zhang X, Wang L and Yao J 2011 *J. Opt. Soc. Am.* B **28** 2186–90
[81] Chen C T, Wang Y B, Wu B C, Wu K C, Zeng W L and Yu L H 1995 *Nature* **374** 322–4
[82] Hu Z G, Higashiyama T, Yoshimura M, Yap Y K, Mori Y and Sasaki T 1998 *Japan. J. Appl. Phys.* **37** L1093–4
[83] Ye N, Zeng W R, Wu B C, Huang X Y and Chen C T 1998 *Z. Kristallogr.–New Cryst. Struct.* **213** 452
[84] Hu Z G, Yoshimura M, Muramatsu K, Mori Y and Sasaki T 2002 *Japan. J. Appl. Phys.* **41** L1131–3
[85] Hellwig H, Liebertz J and Bohaty L 1999 *Solid State Commun.* **109** 249–51
[86] Hellwig H, Liebertz J and Bohaty L 2000 *J. Appl. Phys.* **88** 240–4
[87] Jung S T, Choi D Y and Chung S J 1996 *Mater. Res. Bull.* **31** 1007–10
[88] Halasyamani P S 2004 *Chem. Mater.* **16** 3586–92
[89] Boyd G D, Nassau K, Miller R C, Bond W L and Savage A 1964 *Appl. Phys. Lett.* **5** 234–6
[90] Cohen R E and Krakauer H 1990 *Phys. Rev.* B **42** 6416–23
[91] Isaenko L, Vasilyevva I, Merkulev A, Yelisseyev A and Lobanov L 2005 *J. Cryst. Growth* **275** 217
[92] Isaenko L, Krinitsin P, Vedenyapin V, Yelisseyev A, Merkulev A, Zondy J J and Petrov V 2005 *Cryst. Growth Des.* **5** 1325–9
[93] Abrahams S C and Bernstein J L 1973 *J. Chem. Phys.* **59** 1625–9
[94] Hahn H, Frank G, Klingler W and Meyer A D 1953 *Z. Anorg. Allg. Chem.* **271** 153–70
[95] Kistaiah P, Venudar Y C, Murthy K S, Iyengar L and Krishna K V 1981 *J. Appl. Crystallogr.* **14** 281–4
[96] Lee M H, Yang C H and Jan J H 2004 *Phys. Rev.* B **70** 235110
[97] Stadele M, Moukara M, Majewski J A and Vogl P 1999 *Phys. Rev.* B **59** 10031–43
[98] Tao J M and Perdew J P 2003 *Phys. Rev. Lett.* **91** 146401
[99] Runge E and Gross E K U 1984 *Phys. Rev. Lett.* **52** 997–1000
[100] Chan M K Y and Ceder G 2010 *Phys. Rev. Lett.* **105** 196403
[101] He R, Lin Z S, Zheng T, Huang H and Chen C T 2012 *J. Phys. Condens. Matter* **24** 145503 An alternative method can be seen in [118]
[102] Okeeffe M and Brese N E 1992 *Acta Crystallogr.* B **48** 152–4
[103] Huang H W, Yao J Y, Lin Z S, Wang X Y, He R, Yao W J, Zhai N and Chen C T 2011 *Chem. Mater.* **23** 5457–63
[104] Yan X, Luo S Y, Lin Z S, Yao J Y, He Ran, Yue Y C and Chen C T 2014 *Inorg. Chem.* **53** 1952–4
[105] Meng X Y, Wen X H and Liu G L 2008 *J. Korean Phys. Soc.* **52** 1277–80
[106] Lin Z S, Wang Z Z, Chen C T, Wu I P and Lee M H 2004 *Chem. Phys. Lett.* **399** 125–9
[107] ICSD, 2012-1, Version 1.8.2, by Fachinformatiionszentrum Karlsruhe, Germany
[108] Kang L, Luo S Y, Huang H W, Ye N, Lin Z S, Qin J G and Chen C T 2013 *J. Phys. Chem.* C **117** 25684–92
[109] Kang L, Lin Z S, Qin J G and Chen C T 2013 *Sci. Rep.* **3** 1366
[110] Okorogu A O, Mirov S B, Lee W, Crouthamel D I, Jenkins N, Dergachev A Y, Vodopyanov K L and Badikov V V 1998 *Opt. Commun.* **155** 307–12
[111] Boyd G D, Storz F G, Mcfee J H and Kasper H M 1972 *IEEE J. Quantum Electron.* **8** 900–8
[112] Boyd G D, Buehler E and Storz F G 1971 *Appl. Phys. Lett.* **18** 301–4
[113] Isaenko L, Yelisseyev A, Lobanov S, Titov A, Petrov V, Zondy J J, Krinitsin P, Merkulov A, Vedenyapin V and Smirnova J 2003 *Cryst. Res. Technol.* **38** 379–387
[114] Tang L C, Huang J Y, Chang C S, Lee M H and Liu L Q 2005 *J. Phys.: Condens. Matter* **17** 7275–86
[115] Ren P, Qin J G and Chen C T 2003 *Inorg. Chem.* **42** 8–10
[116] Zhang G, Qin J G, Liu T, Zhu T X, Fu P Z, Wu Y C and Chen C T 2008 *Cryst. Growth Des.* **8** 2946–9
[117] Zhang G, Liu T, Zhu T X, Qin J G, Wu Y C and Chen C T 2008 *Opt. Mater.* **31** 110–3
[118] Liu T, Qin J, Zhang G, Zhu T, Niu F, Wu Y and Chen C 2008 *Appl. Phys. Lett.* **93** 091102
[119] Huang Y, Meng X G, Kang L, Li Y J, Zhong C, Lin Z S, Chen X G and Qin J G 2013 *CrystEngComm* **15** 4196–200
[120] Yelisseyev A, Lin Z S, Starikova M, Isaenko L and Lobanov S 2012 *J. Appl. Phys.* **111** 113507
[121] Lin Z S, Bai L, Liu J, Lee M H, Xu J, Wang X Y and Chen C T 2011 *J. Appl. Phys.* **107** 073721
[122] Lin Z S, Xu L F, Liu L J, Xu J, Lee M H and Chen C T 2010 *Phys. Rev.* B **82** 035124
[123] Lin Z S, Xu L F, Li R K, Wang Z Z, Chen C T, Lee M H, Wang E G and Wang D S 2004 *Phys. Rev.* B **70** 233104
[124] Chen C T *et al* 2012 *Nonlinear Optical Borate Crystals* (Germany: Wiley)
[125] The Materials Genome www.materialsgenome.org